Lanthanide-mediated tuning of electronic and magnetic properties in heterotrimetallic cyclooctatetraenyl multidecker self-assemblies

Zheng Zhou, James Mcneely, Joshua Greenough, Zheng Wei, Haixiang Han, Mathieu Rouzières, Andrey Rogachev, Rodolphe Clérac, Marina Petrukhina

To cite this version:

Zheng Zhou, James Mcneely, Joshua Greenough, Zheng Wei, Haixiang Han, et al.. Lanthanide-mediated tuning of electronic and magnetic properties in heterotrimetallic cyclooctatetraenyl multidecker self-assemblies. Chemical Science, 2022, 10.1039/d2sc00631f. hal-03625892

HAL Id: hal-03625892
https://hal.science/hal-03625892

Submitted on 31 Mar 2022

Lanthanide-mediated tuning of electronic and magnetic properties in heterotrimetallic cyclooctatetraenyl multidecker self-assemblies†

Zheng Zhou,[a] James McNeely,[b] Joshua Greenough,[a] Zheng Wei,[a] Haixiang Han,[c] Mathieu Rouzières,[d] Andrey Yu. Rogachev,*[e] Rodolphe Clérac *[d] and Marina A. Petrukhina *[a]

[a]*Department of Chemistry, University at Albany, State University of New York, Albany, NY 12222, USA. E-mail: mpetrukhina@albany.edu*

[b]*Department of Chemistry, Boston University, Boston, MA, USA*

[c]*Department of Materials Science and Engineering, Cornell University, Ithaca, New York 14853, USA*

[d]*Univ. of Bordeaux, CNRS, Centre de Recherche Paul Pascal, UMR 5031, F-33600, Pessac, France. E-mail: clerac@crpp-bordeaux.cnrs.fr*

[e]*Department of Chemistry, Illinois Institute of Technology, Chicago, IL 60616, USA. E-mail: andrey.rogachev@iit.edu; andrey.rogachev@gmail.com*

Abstract:

The synthesis of a novel family of homoleptic COT-based heterotrimetallic self-assemblies bearing the formula [LnKCa(COT)$_3$(THF)$_3$] (Ln(III) = Gd, Tb, Dy, Ho, Er, Tm, and Yb) is reported followed by their X-ray crystallographic and magnetic characterization. All crystals conform to the monoclinic $P2_1/c$ space group with a slight compression of the unit cell from 3396.4(2) Å^3 to 3373.2(4) Å^3 along the series. All complexes exhibit a triple-decker structure having the Ln(III) and K(I) ions sandwiched by three COT^{2-} ligands with an end-bound {Ca^{2+}(THF)$_3$} moiety to form a non-linear (153.5°) arrangement of three different metals. The COT^{2-} ligands act in a η^8-mode with respect to all metal centers. A detailed structural comparison of this unique set of heterotrimetallic complexes has revealed consistent trends along the series. From Gd to Yb, the Ln to ring-centroid distance decreases from 1.961(3) Å to 1.827(2) Å. In contrast, the separation of K(I) and Ca(II) ions from the COT-centroid (2.443(3) and 1.914(3) Å, respectively) is not affected by the change of Ln(III) ions. The magnetic property investigation of the [LnKCa(COT)$_3$(THF)$_3$] series (Ln(III) = Gd, Tb, Dy, Ho, Er, and Tm) reveals that the Dy, Er, and Tm complexes display slow relaxation of their magnetization, in other words, single-molecule magnet (SMM) properties. This behaviour is dominated by thermally activated (Orbach-like) and quantum tunneling processes for [DyKCa(COT)$_3$(THF)$_3$] in contrast to [ErKCa(COT)$_3$(THF)$_3$], in which the thermally activated and Raman processes appear to be relevant. Details of the electronic structures and magnetic properties of these complexes are further clarified with the help of DFT and *ab initio* theoretical calculations.

Introduction

In recent decades, the design of structural platforms capable of supporting target mixed-metal ion combinations attracted significant interest of synthetic and materials chemists from both fundamental and applied perspectives.[1–4] This attention is not surprising, given the near-infinite number of possible combinations of metals, ligands, and their spatial-orientations. It is precisely this diversity of constitutional and structural possibilities that has given rise to a wide range of physical properties and applications such as single-molecule magnets (SMMs),[5–9] luminescence,[10,11] and catalysis.[12,13] Importantly, with powerful design concepts, the properties of individual metal centers can be modulated through variations of experimental conditions and the structural environment,[14–16] thus entailing novel responsive compounds, which exhibit properties superior in complexity to their homometallic analogues and lower-nuclearity cognates.[17,18]

Despite the expected diversity of high-nuclearity (three or more metal centers) heterometallic complexes, a search of the literature reveals that nearly all reported examples rely on oxygen or nitrogen-based ligands.[6,16,19–21] The vast majority of structurally characterized complexes fall into the broad family of coordination polymers,[22,23] with most of the remaining structural scaffolds being either multinuclear metal clusters[24] or supramolecular networks.[15] Often these structurally complex architectures have been shown to evade rational design,[25] thus thwarting control of their physical properties, particularly in regards to magnetism. This leaves a gap in our fundamental understanding of how multiple metals of different natures interact in an organometallic environment.

One ligand that has shown particular viability for the construction of heterometallic organometallic complexes is the aromatic 10 π electron cyclooctatetraenyl (COT^{2-}) ligand.[26] The success of COT^{2-} arises from its high rotational symmetry[27] and unique ability to bind to metal ions that span a wide range of ionic radii from as large as 1.38 Å (K(I))[28] to as small as 0.605 Å (V(IV)).[29] These favorable properties resulted in the broad use of COT^{2-} in the synthesis of new organometallic complexes of lanthanides.[28,30–32] The interplay of the different oxidation states of lanthanides and the ratio between Ln and COT^{2-} ligands has been efficiently utilized in the preparation of many Ln–COT complexes with interesting magnetic properties,[32,33] including remarkable mixed-ligand SMMs.[33–37]

Considering homometallic organometallic complexes, Ln(IV) ions prefer to be sandwiched by two COT^{2-} rings (1 : 2 ratio, Scheme 1a), as in Ce(COT)$_2$.[38] Complexes of Ln(III) ions with COT^{2-} of a 2 : 3 composition (Scheme 1b) are well known,[31,32,39] with some new members of this type having recently been synthesized and structurally characterized by our group.[40] Furthermore, the addition of substituents to COT ligands has been used to modulate the geometry of such complexes,[41] further enhancing their SMM behaviour.[39,42] In addition, a series of the Ln(II)-based 1D polymers with a 1 : 1 ratio to COT^{2-} has been reported,[43] but their crystal structures remain unknown.

Switching to bimetallic complexes, the 1 : 1 ratio of Ln(III) : K(I) allows balancing the negative charge of COT^{2-} and has been realized in two general structural types. The most popular structural motif is represented by the anionic sandwich [Ln(COT)$_2$]$^-$ with a contact or solvent-separated M(I) ion (Scheme 1c).[44] In 2013, a report on the SMM properties of K[Er(COT)$_2$] drove strong attention to this type of complex.[45] In parallel, the use of bulky COT ligands in such structures has been shown to improve magnetic behaviour.[39,42,46] The second structural type is based on Ln(III)–K(I)–Ln(III)–K(I) tetranuclear species (Scheme 1d), which was initially synthesized and structurally characterized back in 1991 [28] and further investigated due to their SMM properties in 2014.[42] For bimetallic combinations with Ln(II), several products were reported (Scheme 1e),[47–50] in which Eu(II), Tm(II), or Yb(II) is sandwiched by two COT^{2-} anions, and the negative charge is balanced by the side-binding of two M(I) ions.

To date, the highest energy barriers of the Orbach relaxation for the COT-based SMMs have been observed in mononuclear Ln complexes and can be attributed to a fine refinement of their crystal field and local symmetry.[51–54] Although assembling larger molecules containing multiple metal centers is very challenging, such extension could facilitate exchange coupling between metal centers and further enhance magnetic properties.[39,55] Furthermore, introducing more paramagnetic ions could increase the total magnetic moment, which could also improve the blocking temperature of lanthanide-based SMMs.[42]

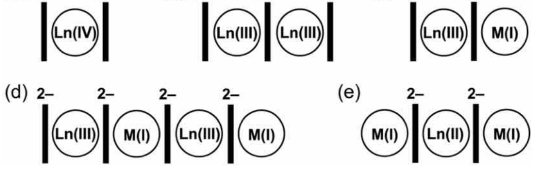

Scheme 1 Depiction of crystallographically characterized homoleptic Ln complexes with the COT^{2-} ligand.

Until now, there have been no COT-based heterotrimetallic complexes reported. Inspired by the above seminal studies, we decided to gradually add structural complexity by increasing the number of unique metal centers from two to three. We targeted the preparation of novel heterotrimetallic homoleptic cyclooctatetraenyl compounds and used Ca(II) as a source of M(II) in addition to Ln(III) and K(I). Herein, we report the synthesis and full characterization of the first heterotrimetallic cyclooctatetraenyl complexes bearing the formula [LnKCa(COT)$_3$(THF)$_3$] (Ln = Gd, Tb, Dy, Ho, Er, Tm, and Yb). Their X-ray crystallographic analysis revealed unique structural features and systematic trends along the series. The magnetic properties of the new set of complexes have been investigated, revealing the SMM behaviour of the Dy, Er, and Tm analogues.

Results and discussion

The preparation of this new class of compounds has been achieved by a facile one-pot synthesis (Scheme 2). The solution of K$_2$COT (3 eq.) was added dropwise to an equimolar mixture of LnCl$_3$ (Ln = Gd, Tb, Dy, Ho, Er, Tm, and Yb) and CaI$_2$ in THF at room temperature. The reaction was allowed to proceed to completion over 24 hours. After removal of the KI and KCl salts by filtration, the products were crystallized using slow diffusion of hexanes to the THF filtrate. Plate-shaped crystals were isolated in good yield after several days (see the ESI† for more details). The X-ray diffraction study confirmed that products are isostructural and conform to a monoclinic $P2_1/c$ space group (Table S8†). Notably, as the ionic radius decreases from Gd to Yb, the unit cell undergoes slight compression with the volume changing from 3396.4(2) to 3373.2(4) Å^3, which is consistent with the observed shortening of the a and c axes.

All complexes contain three metal centers with a ratio of 1 : 1 : 1 to form [LnKCa(COT)$_3$(THF)$_3$] (Ln = Gd (**1-Gd**), Tb (**2-Tb**), Dy (**3-Dy**), Ho (**4-Ho**), Er (**5-Er**), Tm (**6-Tm**), and Yb (**7-Yb**)). The phase purity of **1–7** has been proven by X-ray powder diffraction using Le Bail fit (Fig. S2–S8, Tables S1–S7†). The infrared spectra of the crystalline solids show their close similarity for the series with major bands at 677, 876, 888, and 1030 cm^{-1} (Fig. S1†).

Crystallographic study

Since Dy(III) and Er(III) complexes usually exhibit an interesting magnetic response such as SMM properties, we first performed

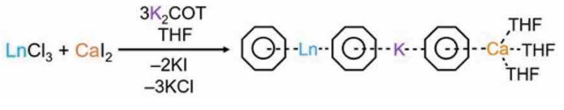

Scheme 2 Preparation of complexes **1–7** (Ln = Gd–Yb).

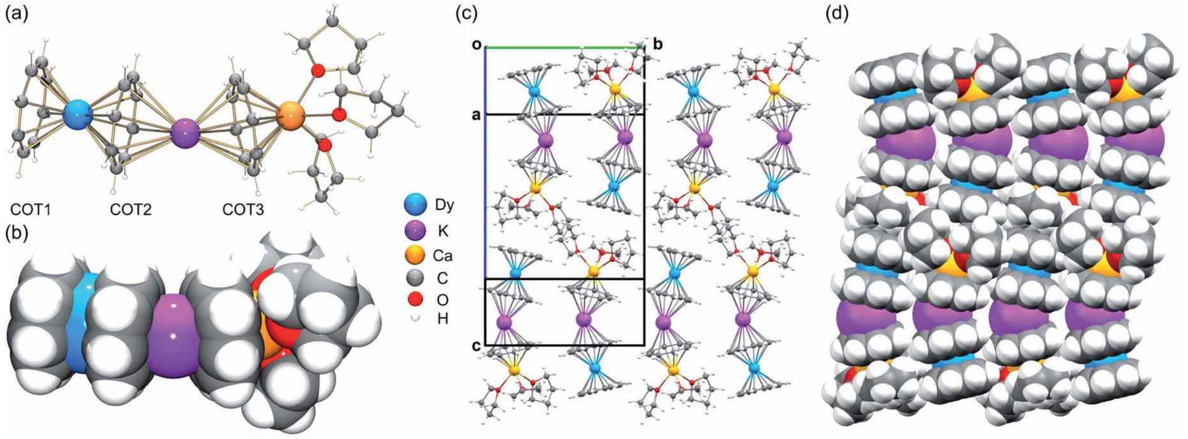

Fig. 1 Crystal structure and solid-state packing of [DyKCa(COT)$_3$(THF)$_3$] (**3-Dy**) at 100 K: (a and c) ball-and-stick and (b and d) space-filling models.

Table 1 Selected bond length distances[a] (Å) and angles (°) in **1–7** along with the Ln(III) ionic radius[b]

	1-Gd	**2-Tb**	**3-Dy**	**4-Ho**	**5-Er**	**6-Tm**	**7-Yb**
Ionic radius[56]	1.053	1.040	1.027	1.015	1.004	0.994	0.985
Ln–COT1	1.913(3)	1.891(2)	1.874(8)	1.859(3)	1.846(2)	1.832(2)	1.827(2)
Ln–COT2	1.961(3)	1.939(2)	1.923(8)	1.907(3)	1.896(2)	1.881(2)	1.871(2)
K–COT2	2.479(3)	2.476(2)	2.478(8)	2.476(3)	2.475(2)	2.476(2)	2.478(2)
K–COT3	2.409(3)	2.407(2)	2.408(8)	2.407(3)	2.408(2)	2.409(2)	2.407(2)
Ca–COT3	1.915(2)	1.914(2)	1.912(8)	1.914(2)	1.913(2)	1.916(2)	1.913(2)
∠Ln–K–Ca	153.47(2)	153.56(1)	153.52(5)	153.56(2)	153.59(1)	153.62(1)	153.62(1)

[a] Values are averaged. [b] The ionic radii correspond to the coordination number 8.

a detailed structural analysis of **3-Dy** and **5-Er** and then used them for comparison with the [LnKCa(COT)$_3$(THF)$_3$] series. In the crystal structures of **3-Dy** (Fig. 1a and b) and **5-Er** (Fig. S13†), the Dy(III) or Er(III) ion is sandwiched by two η^8-coordinated COT^{2-} ligands (COT1 and COT2), with the two rings being almost parallel to each other (0.9° and 0.8°, respectively). This small deviation is commonly seen in [Ln(COT)$_2$]$^-$ complexes with a tilting angle up to 7.9°.[28,31,40,42,45,47] The Dy–C (2.614(8)–2.683(7) Å) and Er–C (2.593(2)–2.644(2) Å) distances are close (Table 1) to those reported in the literature.[33,39,45,46]

In the solid-state structures of **3-Dy** (Fig. 1c and d) and **5-Er** (Fig. S16†), some weak C–H⋯π interactions can be identified along the *c* axis between the open-ended COT1 decks and coordinated THF molecules from neighboring molecules, with the shortest distances of 2.708(5)–2.751(5) Å and 2.693(2)–2.731(2) Å, respectively. The resulting 1D columns are packed in opposite directions with no significant interactions found between the adjacent columns.

A detailed structural comparison of the extended family of complexes **1–7** (see Fig. S9–S15† for analogous complexes) was carried out, revealing consistent trends along the series (Table 1 and Fig. 2).[56] From **1-Gd** to **7-Yb**, the Ln to ring-centroid distance systematically decreases from 1.913(3) Å to 1.827(2) Å and from 1.961(3) Å to 1.871(2) Å (for COT1 and COT2, respectively), which is consistent with the decrease of the Ln(III) ionic radius.[56] The Ln(III) ion sits closer to COT1 than COT2, with the Ln–COT$_{\mathrm{centroid}}$ bond length difference averaging at 0.048 Å. In contrast, the K–COT$_{\mathrm{centroid}}$ and Ca–COT3$_{\mathrm{centroid}}$ (averaged to 1.914(3) Å) distances are not affected by the change of Ln(III) ions. As mentioned, the K(I) to the COT3-centroid distance (averaged to 2.477(3) Å) is shorter than that to COT2 (averaged to 2.408(3) Å). The average Ln–K–Ca angle is 153.6°, which is not affected by the change of lanthanide ions in this series. In the solid-state structures of **1–7** (Fig. S16†), 1D columns are formed

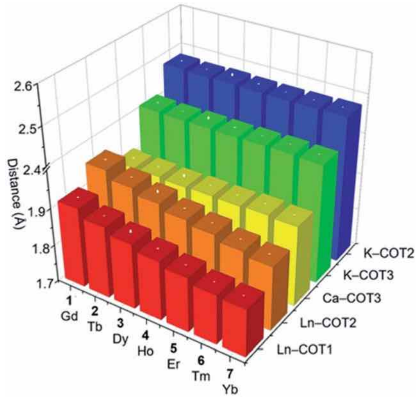

Fig. 2 A 3D chart of the selected M–COT$_{\mathrm{centroid}}$ distances (Å) tabulated in Table 1 for **1–7**.

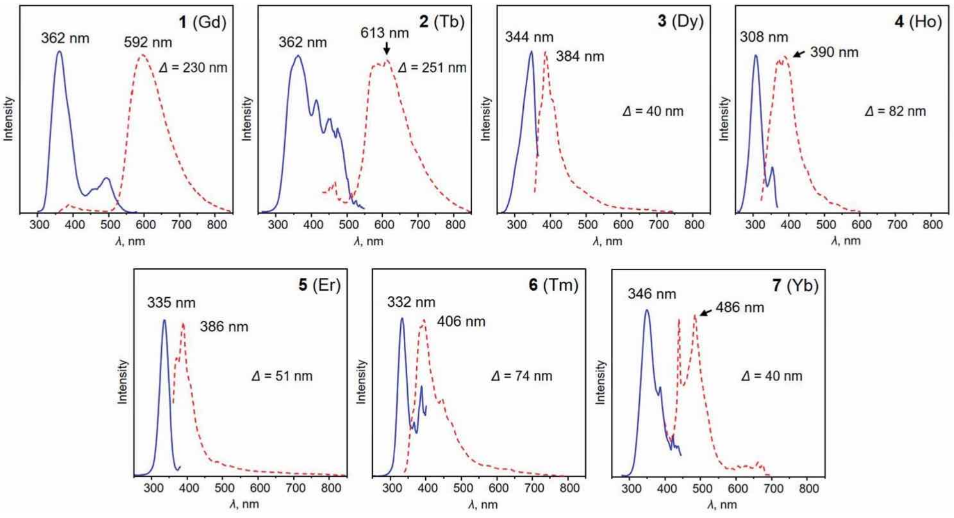

Fig. 3 Photoluminescence excitation (PLE, blue lines) and photoluminescence emission (PL, red dotted lines) spectra of **1–7** in THF at 20 °C.

along the *c* axis through weak C–H···π interactions between COT1 and THF from adjacent molecules (2.692(1)–2.751(5) Å, Table S11†), with no noticeable interactions found between the adjacent columns. The intramolecular Ln–K and Ca–K distances for this series are 4.348(2)–4.440(2) Å and 4.319(2)–4.323(2) Å, respectively (Table S12†). The shortest intermolecular Ln–Ln distances between the columns range from 9.260(2) to 9.277(2) Å. The solid-state packing in **1–7** is tight with the void space (averaged to 11.8 Å^3) being similar for the whole family.

Photoluminescence properties

The heterotrimetallic [LnKCa(COT)$_3$(THF)$_3$] scaffold exhibits great flexibility in accommodating a variety of different lanthanide ions, providing a unique platform for the investigation of the relationship between the lanthanide metal center and optical properties. In this respect, it offers the feasibility to tune the electronic structure of such heterotrimetallic compounds by choosing an appropriate lanthanide metal, since a significant contribution comes from their 4f orbitals. Based on photoluminescence spectroscopy investigation, compounds **1–7** feature similar PL and PLE profiles (Fig. 3). The main excitation wavelengths for this series fall into a relatively narrow range between 308 and 362 nm, whereas the corresponding emission peaks vary broadly from 390 to 592 nm, depending on the lanthanide ion. Specifically, complexes **3–7** (Dy, Ho, Er, Tm, and Yb) demonstrate typical sharp emission profiles with relatively small Stokes shifts ranging from 40 to 82 nm. This stems from the evidence that the optical responses of lanthanide complexes are associated with electron transitions within the 4f^n orbitals, which are shielded by the filled 5s^2 and 5p^2 orbitals. As a result, the ligand field strength cannot significantly affect the energy, thus leading to a small Stokes shift.[57,58] In contrast, complexes **1-Gd** and **2-Tb** exhibit larger Stokes shifts of 230 and 251 nm, respectively. This can be associated with the special position Tb holds among the lanthanide series, as the photoluminescence of Tb-containing complexes results from the 4f–5d transition, while ligand-to-metal charge-transfer (LMCT) is the main driving force for others.[59,60] Similar observations have also been reported for other Tb and Gd-complexes.[61] For example, upon excitation at 350 nm, complex [Tb(Cp)$_3$(THF)] (Cp = cyclopentadienyl) displays a broad photoluminescence band from 545 to 555 nm.[62] Similarly, the [Tb(hfa)$_3$(tppo)$_2$] (hfa = hexafluoroacetylacetonate, tppo = triphenylphosphine oxide) complex synthesized by Hasegawa and co-workers displays photoluminescence at 548 nm upon excitation at 350 nm.[63] The versatility of lanthanide ions results in their unique electronic structures, which can be further used to tune the optical properties, suggesting potential applications in photocatalysis, sensing, and bio-imaging.[64,65]

Magnetic properties

The magnetic properties of complexes **1–6** were studied using dc and ac susceptibility measurements (see the ESI† for more details). Around room temperature, the χ*T* product values are

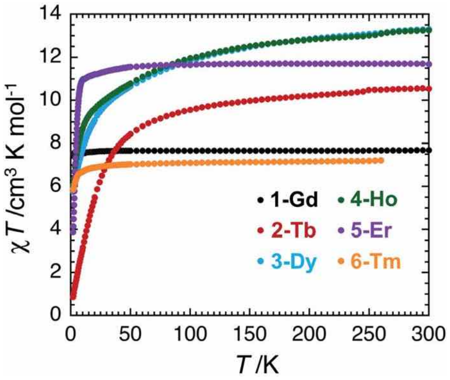

Fig. 4 Temperature dependence of the χ*T* product for **1–6** at 0.1 T (χ, the dc magnetic susceptibility, is defined as *M*/*H* per mole of complex; *M* and *H* being the magnetisation and applied magnetic field, respectively).

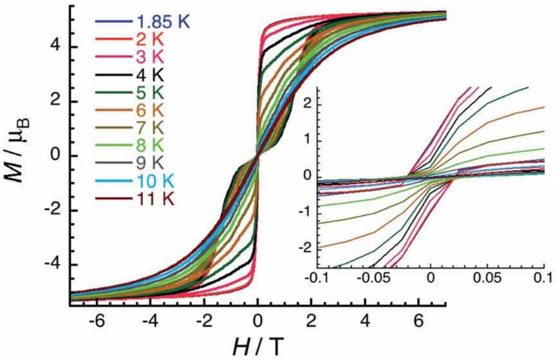

Fig. 5 Field dependence of the magnetisation for **5-Er** at low temperatures between 1.85 and 11 K with applied magnetic field from −7 to 7 T (main) and from −0.1 to 0.1 T (inset). The magnetisation data are shown as a *M versus H* plot with the following field sweep rates: 80 Oe min^{-1} between 0 and 0.1 T, 170 Oe min^{-1} between 0.1 and 0.3 T, 400 Oe min^{-1} between 0.3 and 1 T, 830 Oe min^{-1} between 1 and 2 T, 2800 Oe min^{-1} between 2 and 7 T.

7.7, 10.5, 13.3, 13.3, 11.7 and 7.2 cm^3 K mol^{-1}, respectively, which is coherent with the presence of a single paramagnetic lanthanide site from Gd(III) to Tm(III) (Fig. 4).[66] While the χT value remains quasi constant down to 1.85 K (7.6 cm^3 K mol^{-1}) for **1-Gd**, it shows a more or less marked decrease depending on the Ln(III) center in the experimental temperature window of measurements and reaches the values of 0.86 cm^3 K mol^{-1} for **2-Tb**, 5.76 cm^3 K mol^{-1} for **3-Dy**, 6.05 cm^3 K mol^{-1} for **4-Ho**, 3.88 cm^3 K mol^{-1} for **5-Er**, and 5.91 cm^3 K mol^{-1} for **6-Tm** at 1.85 K. These thermal variations of the χT product confirm the expected presence of a crystal-field splitting for the Tb(III), Dy(III), Ho(III), Er(III), and Tm(III) complexes and a simple Curie paramagnetic behaviour for the Gd(III) analogue.[66] The field dependence of magnetisation was also measured below 8 K (between 0 and 7 T), as shown in Fig. S17–S22.† Under 7 T at 1.85 K, the magnetisations of **1-Gd**, **5-Er**, and **6-Tm** are close to saturation, while an absence of saturation is clearly observed for **2-Tb**, **3-Dy**, and **4-Ho** containing the most magnetically anisotropic Ln(III) ions, reaching values of 3.13, 5.52, and 6.28 μ_B, respectively.

Slow dynamics or blocking of magnetisation was detected by dc measurements only for the Er(III) complex (**5-Er**), which is commonly seen in the reported Er–COT complexes.[33,36,42,45,67–69] Field-dependent magnetisation experiments revealed a typical butterfly shaped magnetic hysteretic loop below 10 K (Fig. 5). The magnetisation at 1.85 K and 7 T clearly saturates to a value of 5.29 μ_B. In the reported [$Er_2(COT'')_3$] (COT″ = 1,4-bis(trimethylsilyl) cyclooctatetraene) complex, a significant magnetic interaction between two close Er(III) ions (Er–Er: 4.11 Å) is observed, resulting in an s-shaped hysteresis loop that closes at 12 K.[42] In contrast, a similar butterfly shaped hysteresis of [$K_2Er_2(COT)_4(THF)_4$] below 12 K is indicative of very weak interactions between the Er(III) ions (Er–Er: 8.12 Å).[42] Hence, the dynamic relaxation process of **5-Er** should not be influenced by the Er⋯Er magnetic interactions based on the long Er–Er distance (9.26 Å) and thus, the relaxation originates from a magnetically isolated Er(III) center.

Ac susceptibility was measured for these compounds in order to probe the magnetisation dynamics and determine the characteristic relaxation time among this family of complexes.

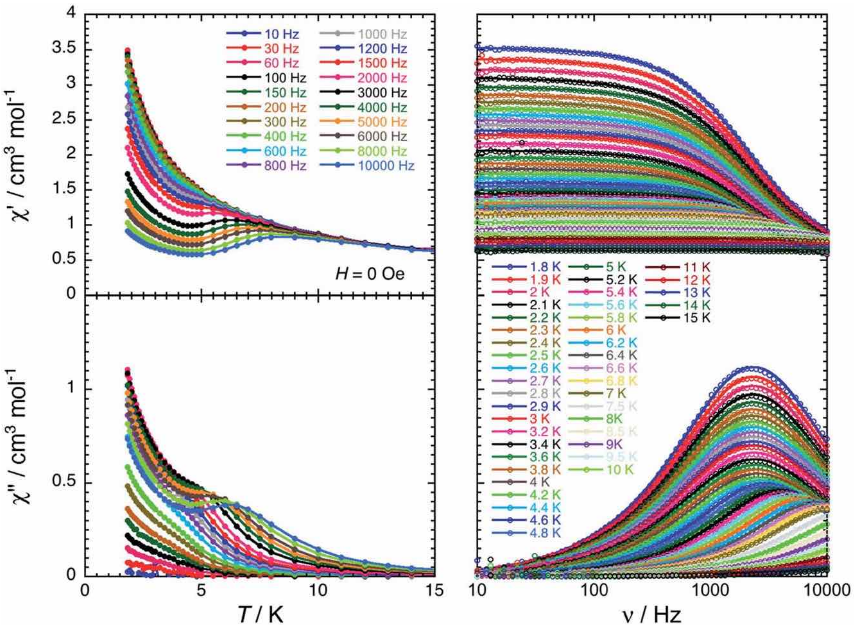

Fig. 6 In-phase (top) and out-of-phase (bottom) components of the molar ac magnetic susceptibility of **3-Dy** measured as a function of temperature at different frequencies (left) and as a function of frequency at different temperatures (right) in zero dc-field. The solid lines on the left plots are a guides for the eye. The solid lines on the right plots are the generalized Debye fits[71,72] of the experimental ac susceptibility data (open dots).

As shown in the following, strong temperature, dc field and frequency dependencies of the ac susceptibility, *i.e.* SMM properties, are observed for **3-Dy**, **5-Er**, and **6-Tm**, while no out-of-phase (χ'') signal is detected for the other analogues. It can be noted here that the magnetic properties of **2-Tb** are comparable to the reported Tb-sandwich with the substituted COT ligands, $[Li(DME)_3][Tb(COT'')_2]$,[70] where no indication of slow magnetic relaxation or hysteresis was observed.

For the Dy(III) complex (**3-Dy**), a single relaxation mode is observed around 2100 Hz at 1.8 K (Fig. 6). This mode is relatively temperature independent up to 3.5 K, as expected for a magnetisation relaxation dominated by quantum tunnelling effects. Above this temperature, the relaxation is temperature dependent and reaches the limit of the experimental ac frequency window (10 kHz) around 7 K. When applying a magnetic field at 5 K, the characteristic relaxation frequency of the relaxation mode shifts from 3500 Hz in zero-dc field to 420 Hz at 0.1 T (Fig. S24 and S25†). The relaxation time of the magnetisation, τ, and its estimated standard deviation (ESD) were deduced as a function of the applied dc-field at 5 K and as a function of the temperature at 0 and 0.1 T (Fig. S29†) from the experimental χ' *versus* ν and χ'' *versus* ν data (Fig. 6, S23 and S26†) fitted to the generalised Debye model.[71,72]

Paramagnetic relaxation is a well-known phenomenon,[73] which finds its origin in four main mechanisms: Raman,[74] direct,[73] thermally activated (Arrhenius or Orbach-like)[73,75] and quantum tunnelling of the magnetisation (QTM)[76–79] processes. Based on the analysis of the relaxation time variations (Fig. S29, see the ESI for equations and detailed discussion, Fig. S28–S30†), both Orbach-like and QTM relaxation mechanisms seem to be present in **3-Dy**. Indeed, the dc-field dependence of τ above 0.1 T could only be potentially reproduced by an Orbach-like relaxation, while at low fields below 0.05 T, the relaxation time is compatible with an H^2 variation expected for QTM or Raman mechanisms. Nevertheless, considering both field and temperature dependences of τ, the modelling of the experimental data favors Orbach-like and QTM relaxations (see the ESI†). It is important to note that the origin of the Orbach-like relaxation with an estimated energy gap of about 43 K is not obvious for a mononuclear Dy complex, and it should certainly be challenged in following theoretical studies (*vide infra*). Even if the relaxation time can be fitted well with the experimental data using five adjustable parameters (Fig. S29†) and similar approaches have already been used for Dy–COT analogous SMMs,[33,39] the physics of the present dynamics might be better described by alternative models, and thus the current analysis should be taken with great caution as any similar modelling of the relaxation for SMMs.

For the Er(III) complex (**5-Er**), the dynamics of the magnetisation is slow enough to be detectable by dc magnetic measurements below 10 K (Fig. 5). Above this temperature, the relaxation time reaches the experimental time scale accessible by the ac susceptibility measurements and thus it can be accurately measured for complex **5-Er**. As shown in Fig. 7, the single relaxation mode observed at 11 K around 0.018 Hz is strongly temperature-dependent and reaches 10 kHz around 37 K. When applying a magnetic field at 27 K, the characteristic frequency of the relaxation mode stays unchanged suggesting that the magnetisation relaxation is dominated by an Orbach-like process in this temperature range. Nevertheless, the ln(τ)

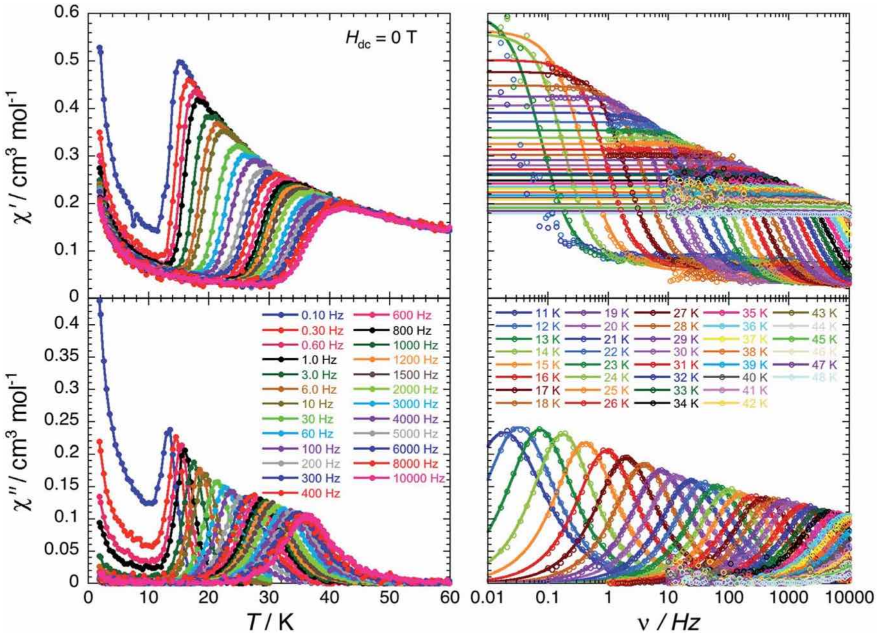

Fig. 7 In-phase (top) and out-of-phase (bottom) components of the molar ac magnetic susceptibility of **5-Er** measured as a function of temperature at different frequencies (left) and as a function of frequency at different temperatures (right) in zero dc-field. The solid lines on the left plots are a guide for the eye. The solid lines on the right plots are the generalized Debye fits[71,72] of the experimental ac susceptibility data (open dots).

vs. T^{-1} plot (Fig. S30†) is not perfectly linear revealing a departure from a simple thermally activated process. A second relaxation pathway should thus be considered. In zero-dc field, only Raman and QTM are active processes but only a model considering Raman and Orbach-like relaxations was able to fit all the experimental data (Fig. S30†).[45] It is worth mentioning that the characteristics of the Orbach-like process (Δ/k_B = 287(16) K) are indeed similar to those estimated in the related Er–COT complexes.[33,42,45]

In the case of the Tm(III) analogue (**6-Tm**), ac measurements reveal a broad relaxation mode (Fig. S31 and S32†), which is weakly temperature dependent and disappears rapidly when a magnetic field is applied suggesting a dominant quantum relaxation.

Thus, despite structural similarity of complexes **1–7**, variations in magnetic behaviour have been clearly observed, prompting comprehensive theoretical investigation of the electronic structures and magnetic properties.

Calculations of electronic structures and magnetic properties

In order to gain further insights into the periodic trends observed in the electronic structures and magnetic properties of the target systems, DFT and *ab initio* calculations were performed with the ORCA[80–82] electronic structure suite. First, we analysed the correlation between geometrical and electronic structures by considering nephelauxetic and relativistic nephelauxetic reductions for the series using strongly correlated multireference perturbation theory of the second order in the NEVPT2 variant (Fig. 8). A similar approach has been recently used by Aravena *et al.*[83] It can be seen that both reductions increase when moving from **1-Gd** to **7-Yb**, which suggests that the covalency is slightly decreased across the series as the ionic radius is reduced.

The trend is also supported by atomic charges and atomic orbital populations calculated within the NBO/NPA framework at both PBE0 and CASSCF(n,7) levels (Table 2). Both sets suggest that the covalent component of the bonding is best described as the interaction between the π-system of the COT ligand and the Ln 5d shell, although the strength of these bondings appeared to be nearly constant from **1-Gd** to **6-Tm**. Average C_{COT1}–Ln Wiberg bond orders (WBOs) of 0.19–0.20 are observed for **1–6**, with corresponding WBOs of 0.15–0.16 for C_{COT2}–Ln bonding contacts. The tendency in bond orders correlates well with that observed in natural charges of the Ln centers (Table 2). The nature of the bonding was further confirmed by the second-order perturbation analysis of the Fock matrix in the NBO basis. It was found that the population of 5d shell along the series correlates with the donor–acceptor stabilization energies between the π-system of COT and the 5d atomic orbitals of Ln.

Table 2 Natural population analysis as applied to DFT and CASSCF(n,7) results

	CASSCF(n,7)				DFT			
System	Charge	4f	5d	6s	Charge	4f	5d	6s
1-Gd	1.50	7.01	1.32	0.11	1.31	7.06	1.44	0.11
2-Tb	1.47	8.01	1.34	0.11	1.28	8.08	1.45	0.12
3-Dy	1.47	9.01	1.34	0.12	1.27	9.09	1.44	0.12
4-Ho	1.47	10.01	1.34	0.12	1.29	10.05	1.46	0.12
5-Er	1.46	11.00	1.34	0.12	1.29	11.05	1.46	0.12
6-Tm	1.46	12.00	1.35	0.12	1.27	12.08	1.45	0.13
7-Yb	1.47	13.00	1.34	0.12	1.22	13.21	1.36	0.13

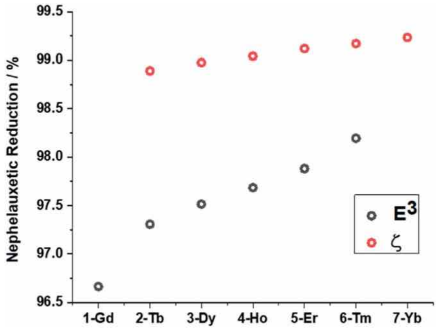

Fig. 8 Nephelauxetic (black) and relativistic nephelauxetic reductions (red) calculated at the NEVPT2(n,7) level.

Notably, calculations clearly indicated **7-Yb** as an outlier. A large increase in excess 4f population and a corresponding decrease in the 5d occupation were observed for this system. Looking at the donor–acceptor interactions between the Yb(III) center and the COT^{2-} π-systems, two notably occupied formally virtual lone valence orbitals, namely 5d–4f hybrids, were found (Fig. 9), thus showing an involvement of the f-shell in the bonding. The second-order delocalization stabilization energy imparted by COT^{2-} π-orbitals to these two acceptors was calculated to be 4.2 kcal mol^{-1}.

This unusual electronic structure of **7-Yb** was further confirmed by *ab initio* ligand field theory (AILFT[84]) analysis of the systems. The 4f shell splitting diagrams computed at the NEVPT2(n,7)/QDPT level of theory are presented in Fig. 10. Notably, a striking discontinuity in the progression of the E_{2u} (based on the D_{8h} symmetry) energy was observed for **7-Yb**. The MAD of these orbital energies for **1-Gd** to **6-Tm** is 52 cm^{-1} when referring to the barycenter. In the case of **7-Yb**, however, this is more than 660 cm^{-1} above the **1–6** barycenter. This strongly hints at orbital interactions with the shell.

Importantly, calculations of the magnetic properties performed at the NEVPT2(n,7)/QDPT level showed good agreement

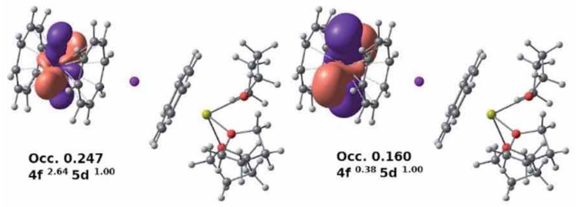

Fig. 9 Two notably occupied formally virtual lone valence 5d–4f hybrid orbitals for the **7-Yb** system (PBE0/SARC2-ZORA-QZVP/ZORA).

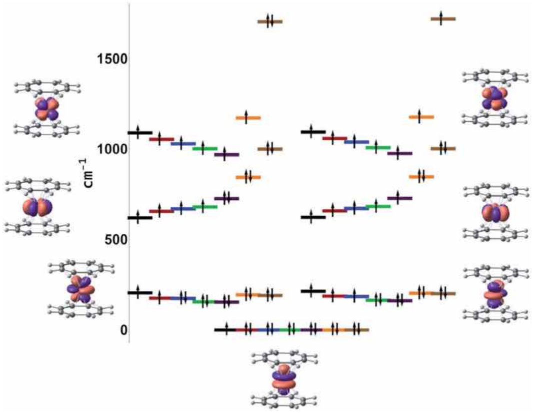

Fig. 10 NEVPT2(n,7)/QDPT AILFT f-orbital splitting (black = Gd, red = Tb, blue = Dy, green = Ho, purple = Er, orange = Tm, brown = Yb).

with experimental results (see Fig. S33–S38†). The calculated room temperature χT products of 7.8, 11.2, 13.8, 13.4, 11.1, and 6.5 cm^3 K mol^{-1} for **1–6**, respectively, agree well with experimentally measured values of 7.7, 10.5, 13.3, 13.3, 11.7, and 7.2 cm^3 K mol^{-1} for the corresponding systems. The reduction in magnetisation at lower temperatures is also reproduced by the computational model. These reductions are due to depopulation of excited levels, and their reproduction clearly indicates that the theoretical model used in this study correctly captures the splitting in the ground state manifold.

For the next step, the CASSCF(n,7)/QDPT/SINGLE_ANISO[85–87] approach was used to investigate the ground state multiplets of the series in order to shed light on the relaxation mechanisms for **3-Dy** and **5-Er**. Notably, the blocking diagram for **5-Er** (Fig. 11) with an energy gap of 272 K between the $M_J = 15/2$ and $M_J = 13/2$ state is similar to the diagram recently reported by Ungur *et al.*[33] for the highly symmetrical Ln–COT^{2-} sandwich-like systems. The transverse moments connecting the $J_z = 15$ to $J_z = -15$, -13 states are very small, thus suggesting extremely small Orbach and QTM rates and increasing the blocking temperature. This argument is also bolstered by the axiality of the effective g-values for the $J_z = \pm 15$, ± 13 multiplets (see the ESI, Table S14†).

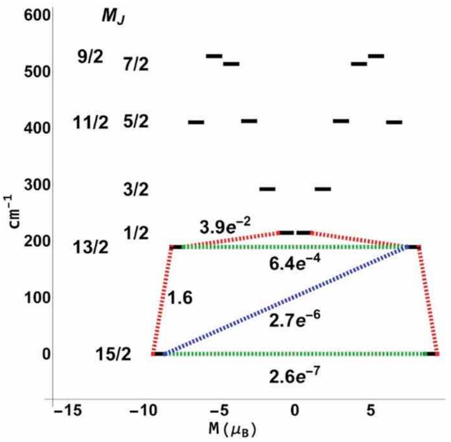

Fig. 11 Blocking diagram from CASSCF(9,7)/QDPT/SINGLE_ANISO calculations for **5-Er**. Blue lines correspond to Orbach relaxation mechanisms, green lines correspond to quantum tunneling of magnetisation, and red lines correspond to the most likely pathway.

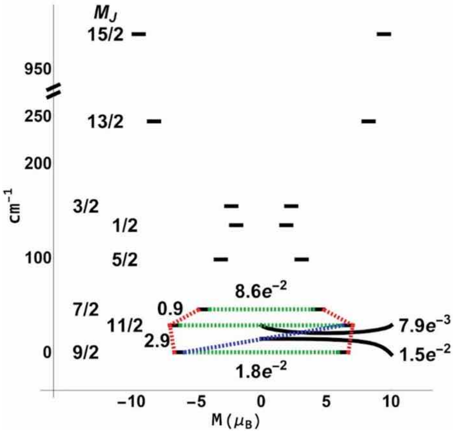

Fig. 12 Blocking diagram from CASSCF(9,7)/QDPT/SINGLE_ANISO calculations for **3-Dy**. Blue lines correspond to Orbach relaxation mechanisms, green lines correspond to quantum tunneling of magnetisation, and red lines correspond to the most likely pathway.

While the features of the multiplet spectrum for **3-Dy** with an energy gap of 41 K between the ground and the first excited microstates (Fig. 12) are qualitatively similar to those reported by Ungur *et al.* for the symmetric Dy–COT^{2-} complexes, the QTM and Orbach transverse moments calculated in this work are $\sim\frac{1}{2}$ of those calculated in ref. 87. Given that the spin-relaxation processes approximately scale as the square of the transverse moment connecting states, the Orbach and QTM rates in the **3-Dy** system can be reliably considered as $\sim\frac{1}{4}$ of those in the symmetric Dy–COT^{2-} molecular species. This reduction in QTM and Orbach rates gives a direct support to the enhanced energy gap derived in this study.

Conclusions

A novel family of homoleptic cyclooctatetraenyl heterotrimetallic complexes, [LnKCa(COT)$_3$(THF)$_3$], has been synthesized and fully characterized using X-ray diffraction, spectroscopy and magnetic susceptibility measurements. Their unique triple-decker molecular structure with Ln(III) and K(I) ions sandwiched by three COT^{2-} ligands with an end-bound {Ca^{2+}(THF)$_3$} moiety adopts a bent arrangement of three different metals. Systematic changes in the geometrical parameters are clearly observed along the series, consistent with the ionic radii decrease from Gd to Yb. The magnetic properties study of the [LnKCa(COT)$_3$(THF)$_3$] family (Ln(III) = Gd, Tb, Dy, Ho, Er, and Tm) revealed the single-molecule magnet (SMM) properties of the Dy, Er, and Tm analogues. Theoretical modeling at the density functional and *ab initio* levels of theory allowed a clear establishment of the magneto-structural correlations, thus bridging geometrical parameters, electronic structures and magnetic behavior of these unique heterotrimetallic triple-decker COT complexes. Competition between the Orbach relaxation mechanism and quantum tunneling of magnetisation was investigated with the help of multireference perturbation theory followed by the construction of corresponding blocking diagrams. The multifaceted nature of magnetic relaxation in these systems was confirmed, thus being in a good agreement with experimental observations. The accuracy of theoretical calculations was supported by precise reproduction of experimental χT curves.

Importantly, the new heterotrimetallic scaffold accommodating axially aligned metal ions from groups 1, 2 and 3 in three different oxidation states provide new synthetic strategies for building multimetallic SMMs and tuning their intramolecular magnetic interactions. The designed structural organization of the heterotrimetallic complexes suggests that the controlled replacement or elimination of the THF molecules could be the first step toward one-dimensional organometallic frameworks with bridging COT ligands. For the next step, title trimetallic oligomers could serve as unique precursors for controlled metal replacement of the M(I) and M(II) sites to afford polymeric or hetero-spin $\{\mathrm{Ln(COT)M(COT)}\}_n$ chains incorporating 3d or 4d metal ions that could display unusual and advanced SMM behaviour.[72]

Financial support of this work from the U.S. National Science Foundation, CHE-2003411, is gratefully acknowledged (M. A. P.). R. C. thanks the University of Bordeaux, the Région Nouvelle Aquitaine, Quantum Matter Bordeaux, the GdR MCM-2

1 G. A. Timco, T. B. Faust, F. Tuna and R. E. P. Winpenny, *Chem. Soc. Rev.*, 2011, **40**, 3067–3075.

2 G. Kumar and R. Gupta, *Chem. Soc. Rev.*, 2013, **42**, 9403–9453.

3 R. J. Wilson, N. Lichtenberger, B. Weinert and S. Dehnen, *Chem. Rev.*, 2019, **119**, 8506–8554.

4 J. A. Chipman and J. F. Berry, *Chem. Rev.*, 2020, **120**, 2409–2447.

5 D. N. Woodruff, R. E. P. Winpenny and R. A. Layfield, *Chem. Rev.*, 2013, **113**, 5110–5148.

6 C. Papatriantafyllopoulou, E. E. Moushi, G. Christou and A. J. Tasiopoulos, *Chem. Soc. Rev.*, 2016, **45**, 1597–1628.

7 R. Sessoli and A. K. Powell, *Coord. Chem. Rev.*, 2009, **253**, 2328–2341.

8 F.-S. Guo, A. K. Bar and R. A. Layfield, *Chem. Rev.*, 2019, **119**, 8479–8505.

9 C. A. Gould, K. R. McClain, D. Reta, J. G. C. Kragskow, D. A. Marchiori, E. Lachman, E. S. Choi, J. G. Analytis, R. D. Britt, N. F. Chilton, B. G. Harvey and J. R. Long, *Science*, 2022, **375**, 198–202.

10 S. Das, K. S. Bejoymohandas, A. Dey, S. Biswas, M. L. P. Reddy, R. Morales, E. Ruiz, S. Titos-Padilla, E. Colacio and V. Chandrasekhar, *Chem.–Eur. J.*, 2015, **21**, 6449–6464.

11 K. Kumar, S. Chorazy, K. Nakabayashi, H. Sato, B. Sieklucka and S. Ohkoshi, *J. Mater. Chem. C*, 2018, **6**, 8372–8384.

12 J. A. Mata, F. E. Hahn and E. Peris, *Chem. Sci.*, 2014, **5**, 1723–1732.

13 P. Buchwalter, J. Rosé and P. Braunstein, *Chem. Rev.*, 2015, **115**, 28–126.

14 K. L. Harriman and M. Murugesu, *Acc. Chem. Res.*, 2016, **49**, 1158–1167.

15 T. J. Sørensen and S. Faulkner, *Acc. Chem. Res.*, 2018, **51**, 2493–2501.

16 M. Pan, W.-M. Liao, S.-Y. Yin, S.-S. Sun and C.-Y. Su, *Chem. Rev.*, 2018, **118**, 8889–8935.

17 M. Zhu, L. Li and J.-P. Sutter, *Inorg. Chem. Front.*, 2016, **3**, 994–1003.

18 O. A. Ejegbavwo, A. A. Berseneva, C. R. Martin, G. A. Leith, S. Pandey, A. J. Brandt, K. C. Park, A. Mathur, S. Farzandh, V. V. Klepov, B. J. Heiser, M. Chandrashekhar, S. G. Karakalos, M. D. Smith, S. R. Phillpot, S. Garashchuk, D. A. Chen and N. B. Shustova, *Chem. Sci.*, 2020, **11**, 7379–7389.

19 L. V. Meyer, F. Schönfeld and K. Müller-Buschbaum, *Chem. Commun.*, 2014, **50**, 8093–8108.

20 H. Han, J. C. Carozza, A. P. Colliton, Y. Zhang, Z. Wei, A. S. Filatov, Y. S. Chen, M. Alkan, A. Y. Rogachev and E. V. Dikarev, *Angew. Chem.*, 2020, **132**, 9711–9717.

21 H. Han, J. C. Carozza, Z. Zhou, Y. Zhang, Z. Wei, A. M. Abakumov, A. S. Filatov, Y.-S. Chen, D. J. SantaLucia,

J. F. Berry and E. V. Dikarev, *J. Am. Chem. Soc.*, 2020, **142**, 12767–12776.

22 W. Liu, Y. Song, Y. Li, Y. Zou, D. Dang, C. Ni and Q. Meng, *Chem. Commun.*, 2004, 2348–2349.

23 Y. Song, C.-B. Tian, Z.-F. Wu and X.-Y. Huang, *New J. Chem.*, 2018, **42**, 5096–5101.

24 M. Shieh, S.-F. Lin, Y.-W. Guo, M.-H. Hsu and Y.-W. Lai, *Organometallics*, 2004, **23**, 5182–5187.

25 X.-Y. Chang, G.-T. Xu, B. Cao, J.-Y. Wang, J.-S. Huang and C.-M. Che, *Chem. Sci.*, 2017, **8**, 7815–7820.

26 T. J. Katz, *J. Am. Chem. Soc.*, 1960, **82**, 3784–3785.

27 T. Nishinaga, T. Ohmae and M. Iyoda, *Symmetry*, 2010, **2**, 76–97.

28 J. Xia, Z. Jin and W. Chen, *J. Chem. Soc., Chem. Commun.*, 1991, 1214–1215.

29 R. G. Swisher, E. Sinn, G. A. Brewer and R. N. Grimes, *J. Am. Chem. Soc.*, 1983, **105**, 2079–2080.

30 R. G. Hayes and J. L. Thomas, *J. Am. Chem. Soc.*, 1969, **91**, 6876.

31 C. W. DeKock, S. R. Ely, T. E. Hopkins and M. A. Brault, *Inorg. Chem.*, 1978, **17**, 625–631.

32 P. Poremba and F. T. Edelmann, *J. Organomet. Chem.*, 1998, **553**, 393–395.

33 L. Ungur, J. J. Le Roy, I. Korobkov, M. Murugesu and L. F. Chibotaru, *Angew. Chem., Int. Ed.*, 2014, **53**, 4413–4417.

34 J. D. Hilgar, M. G. Bernbeck, B. S. Flores and J. D. Rinehart, *Chem. Sci.*, 2018, **9**, 7204–7209.

35 S.-D. Jiang, B. W. Wang, H. L. Sun, Z. M. Wang and S. Gao, *J. Am. Chem. Soc.*, 2011, **133**, 4730–4733.

36 S.-M. Chen, J. Xiong, Y.-Q. Zhang, Q. Yuan, B.-W. Wang and S. Gao, *Chem. Sci.*, 2018, **9**, 7540–7545.

37 L. Münzfeld, C. Schoo, S. Bestgen, E. Moreno-Pineda, R. Köppe, M. Ruben and P. W. Roesky, *Nat. Commun.*, 2019, **10**, 3135.

38 A. Greco, S. Cesca and W. Bertolini, *J. Organomet. Chem.*, 1976, **113**, 321–330.

39 J. J. Le Roy, M. Jeletic, S. I. Gorelsky, I. Korobkov, L. Ungur, L. F. Chibotaru and M. Murugesu, *J. Am. Chem. Soc.*, 2013, **135**, 3502–3510.

40 J. Greenough, Z. Zhou, Z. Wei and M. A. Petrukhina, *Dalton Trans.*, 2019, **48**, 5614–5620.

41 V. Lorenz, S. Blaurock, C. G. Hrib and F. T. Edelmann, *Organometallics*, 2010, **29**, 4787–4789.

42 J. J. Le Roy, L. Ungur, I. Korobkov, L. F. Chibotaru and M. Murugesu, *J. Am. Chem. Soc.*, 2014, **136**, 8003–8010.

43 T. Tsuji, N. Hosoya, S. Fukazawa, R. Sugiyama, T. Iwasa, H. Tsunoyama, H. Hamaki, N. Tokitoh and A. Nakajima, *J. Phys. Chem. C*, 2014, **118**, 5896–5907.

44 K. O. Hodgson, F. Mares, D. F. Starks and A. Streitwieser, *J. Am. Chem. Soc.*, 1973, **95**, 8650–8658.

45 K. R. Meihaus and J. R. Long, *J. Am. Chem. Soc.*, 2013, **135**, 17952–17957.

46 M. Jeletic, P.-H. Lin, J. J. Le Roy, I. Korobkov, S. I. Gorelsky and M. Murugesu, *J. Am. Chem. Soc.*, 2011, **133**, 19286–19289.

47 S. A. Kinsley, A. Streitwieser and A. Zalkin, *Organometallics*, 1985, **4**, 52–57.

48 W. J. Evans, J. L. Shreeve and J. W. Ziller, *Polyhedron*, 1995, **14**, 2945–2951.

49 K. Kawasaki, R. Sugiyama, T. Tsuji, T. Iwasa, H. Tsunoyama, Y. Mizuhata, N. Tokitoh and A. Nakajima, *Chem. Commun.*, 2017, **53**, 6557–6560.

50 J. Moutet, J. Schleinitz, L. La Droitte, M. Tricoire, F. Pointillart, F. Gendron, T. Simler, C. Clavaguéra, B. Le Guennic, O. Cador and G. Nocton, *Angew. Chem., Int. Ed.*, 2021, **60**, 6042–6046.

51 C. A. P. Goodwin, F. Ortu, D. Reta, N. F. Chilton and D. P. Mills, *Nature*, 2017, **548**, 439–442.

52 F.-S. Guo, B. M. Day, Y.-C. Chen, M.-L. Tong, A. Mansikkamäki and R. A. Layfield, *Angew. Chem., Int. Ed.*, 2017, **56**, 11445–11449.

53 F.-S. Guo, B. M. Day, Y.-C. Chen, M.-L. Tong, A. Mansikkamäki and R. A. Layfield, *Science*, 2018, **362**, 1400–1403.

54 C. A. Gould, K. R. McClain, J. M. Yu, T. J. Groshens, F. Furche, B. G. Harvey and J. R. Long, *J. Am. Chem. Soc.*, 2019, **141**, 12967–12973.

55 J. D. Rinehart, M. Fang, W. J. Evans and J. R. Long, *J. Am. Chem. Soc.*, 2011, **133**, 14236–14239.

56 R. D. Shannon, *Acta Crystallogr., Sect. A: Cryst. Phys., Diffr., Theor. Gen. Crystallogr.*, 1976, **32**, 751–767.

57 Y. Hasegawa, *Bull. Chem. Soc. Jpn.*, 2014, **87**, 1029–1057.

58 Y. Hasegawa, Y. Kitagawa and T. Nakanishi, *NPG Asia Mater.*, 2018, **10**, 52–70.

59 S. Faulkner, S. J. A. Pope and B. P. Burton-Pye, *Appl. Spectrosc. Rev.*, 2005, **40**, 1–31.

60 P. P. Ferreira da Rosa, Y. Kitagawa and Y. Hasegawa, *Coord. Chem. Rev.*, 2020, **406**, 213153.

61 M. Bortoluzzi, G. Paolucci, S. Polizzi, L. Bellotto, F. Enrichi, S. Ciorba and B. S. Richards, *Inorg. Chem. Commun.*, 2011, **14**, 1762–1766.

62 H. G. Brittain, J. H. Meadows and W. J. Evans, *Organometallics*, 1983, **2**, 1661–1665.

63 K. Yanagisawa, T. Nakanishi, Y. Kitagawa, T. Seki, T. Akama, M. Kobayashi, T. Taketsugu, H. Ito, K. Fushimi and Y. Hasegawa, *Eur. J. Inorg. Chem.*, 2015, **2015**, 4769–4774.

64 J.-C. G. Bünzli, *Chem. Rev.*, 2010, **110**, 2729–2755.

65 Y. Qiao and E. J. Schelter, *Acc. Chem. Res.*, 2018, **51**, 2926–2936.

66 L. Sorace and D. Gatteschi, in *Lanthanides and Actinides in Molecular Magnetism*, ed. R. A. Layfield and M. Murugesu, Wiley, Weinheim, 2015.

67 S. D. Jiang, S. S. Liu, L. N. Zhou, B. W. Wang, Z. M. Wang and S. Gao, *Inorg. Chem.*, 2012, **51**, 3079–3087.

68 J. J. Le Roy, I. Korobkov and M. Murugesu, *Chem. Commun.*, 2014, **50**, 1602–1604.

69 J. D. Hilgar, B. S. Flores and J. D. Rinehart, *Chem. Commun.*, 2017, **53**, 7322–7324.

70 V. Lorenz, P. Liebing, M. Böhme, A. Buchholz, W. Plass, N. Geue, L. Hilfert, S. Busse, F. Engelhardt, C. G. Hrib and F. T. Edelmann, *Eur. J. Inorg. Chem.*, 2017, 4840–4849.

71 K. S. Cole and R. H. Cole, *J. Chem. Phys.*, 1941, **9**, 341–351.

72 D. Reta and N. F. Chilton, *Phys. Chem. Chem. Phys.*, 2019, **21**, 23567–23575.

73 K. N. Shrivastava, *Phys. Status Solidi B*, 1983, **117**, 437–458.

74 J. H. Van Vleck, *Phys. Rev.*, 1940, **57**, 426–447.

75 W. Wernsdorfer, M. Murugesu, A. J. Tasiopoulos and G. Christou, *Phys. Rev. B: Condens. Matter Mater. Phys.*, 2005, **72**, 212406.

76 A. Abragam and B. Bleaney, *Electron Paramagnetic Resonance of Transition Ions*, Dover, New York, 1986.

77 L. Lecren, W. Wernsdorfer, Y.-G. Li, O. Roubeau, H. Miyasaka and R. Clérac, *J. Am. Chem. Soc.*, 2005, **127**, 11311–11317.

78 D. Gatteschi, R. Sessoli and J. Villain, *Molecular Nanomagnets*, Oxford University Press, Oxford, 2006.

79 M. Ding, A. K. Hickey, M. Pink, J. Telser, D. L. Tierney, M. Amoza, M. Rouzières, T. J. Ozumerzifon, W. A. Hoffert, M. P. Shores, E. Ruiz, R. Clérac and J. M. Smith, *Chem.–Eur. J.*, 2019, **25**, 10625–10632.

80 F. Neese, *Wiley Interdiscip. Rev. Comput. Mol. Sci.*, 2012, **2**, 73–78.

81 F. Neese, *Wiley Interdiscip. Rev. Comput. Mol. Sci.*, 2018, **8**, e1327.

82 F. Neese, F. Wennmohs, U. Becker and C. Riplinger, *J. Chem. Phys.*, 2020, **152**, 224108.

83 D. Aravena, M. Atanasov and F. Neese, *Inorg. Chem.*, 2016, **55**, 4457–4469.

84 M. Atanasov, D. Ganyushin, K. Sivalingam and F. Neese, in *Molecular Electronic Structures of Transition Metal Complexes II*, Springer, Berlin, Heidelberg, 2012, pp. 149–220.

85 L. F. Chibotaru and L. Ungur, *J. Chem. Phys.*, 2012, **137**, 064112.

86 N. Iwahara, L. Ungur and L. F. Chibotaru, *Phys. Rev. B*, 2018, **98**, 054436.

87 L. Ungur and L. F. Chibotaru, *Chem.–Eur. J.*, 2017, **23**, 3708–3718.

Supporting Information

I. Experimental Details

Materials and Methods

All manipulations were carried out using break-and-seal and glove-box techniques[1] under an atmosphere of argon. Tetrahydrofuran (THF) and hexanes were (Sigma-Aldrich) were dried over Na/benzophenone and distilled prior to use. THF-d_8 (Sigma Aldrich) was dried over NaK_2 alloy and vacuum-transferred. Cyclooctatetraene (COT, 98%), potassium (98%), CaI_2 (99.95%), and $TmCl_3$ (99%) were purchased from Sigma Aldrich and used as received. $GdCl_3$ (99.9%), $TbCl_3$ (99.9%), $DyCl_3$ (99.9%), $HoCl_3$ (99.9%), $ErCl_3$ (99.9%), and $YbCl_3$ (99.9%) were purchased from Strem Chemicals and used as received. K_2COT was prepared as described previously.[2] Attenuated total reflection (ATR) spectra were recorded on a Perkin-Elmer Spectrum 100 FT-IR spectrometer. Photoluminescence (PL) measurements were performed on a Horiba Fluoromax 4 spectrometer. The X-ray powder diffraction data were collected on a Bruker D8 Advance diffractometer (Cu Kα radiation, focusing Göbel Mirror, LynxEye one-dimensional detector, a step of 0.02° 2θ, 20 °C). The crystalline samples under investigation were ground under Ar in the glove-box and placed in the dome-like airtight zero background holders. Le Bail fit for powder diffraction patterns was performed using TOPAS, version 4 software package (Bruker AXS, 2006).

[GdKCa(COT)$_3$(THF)$_3$] (1-Gd)

CaI_2 (16 mg, 0.055 mmol) and $GdCl_3$ (15 mg, 0.055 mmol) were stirred in THF (5.0 mL) under an argon atmosphere at 25 °C for 24 hours. Slow addition of K_2COT (30 mg, 0.17 mmol, in 2.0 mL of THF) to a violently stirred solution produced a cloudy yellow mixture with a large amount of white precipitate formed in 30 minutes. The mixture was allowed to stir under an argon atmosphere at 25 °C for 48 hours to complete the reaction. The suspension was then filtered, and the yellow filtrate was layered with 2.5 mL of anhydrous hexanes. The ampule was sealed under argon and stored at 5 °C. Orange-yellow blocks were present in good yield after 5 days. Yield: 34 mg, 80%. ATR-IR: 677, 876, 888, 1030 cm^{-1}.

[TbKCa(COT)$_3$(THF)$_3$] (2-Tb)

CaI_2 (16 mg, 0.055 mmol) and $TbCl_3$ (15 mg, 0.055 mmol) were stirred in THF (5.0 mL) under an argon atmosphere at 25 °C for 24 hours. Slow addition of K_2COT (30 mg, 0.17 mmol, in 2.0 mL of THF) to a violently stirred solution produced a cloudy yellow mixture with a large amount of white precipitate formed in 30 minutes. The mixture was allowed to stir under an argon atmosphere at 25 °C for 48 hours to complete the reaction. The suspension was filtered, and the yellow-orange filtrate was layered with 2.5

mL of anhydrous hexanes. The ampule was sealed under argon and stored at 5 °C. Yellow blocks were present in good yield after 4 days. Yield: 30 mg, 70%. ATR-IR: 677, 876, 888, 1030 cm^{-1}.

[DyKCa(COT)$_3$(THF)$_3$] (3-Dy)

CaI$_2$ (16 mg, 0.055 mmol) and DyCl$_3$ (15 mg, 0.055 mmol) were stirred in THF (5.0 mL) under an argon atmosphere at 25 °C for 24 hours. Slow addition of K$_2$COT (30 mg, 0.17 mmol, in 2.0 mL of THF) to a violently stirred solution produced a cloudy yellow solution with a large amount of white precipitate formed in 30 minutes. The mixture was allowed to stir under an argon atmosphere at 25 °C for 48 hours to complete the reaction. The suspension was filtered, and the yellow filtrate was layered with 2.5 mL of anhydrous hexanes. The ampule was sealed under argon and stored at 5 °C. Yellow blocks were present in good yield after 3 days. Yield: 34 mg, 80%. ATR-IR: 677, 876, 888, 1030 cm^{-1}.

[HoKCa(COT)$_3$(THF)$_3$] (4-Ho)

CaI$_2$ (16 mg, 0.055 mmol) and HoCl$_3$ (15 mg, 0.055 mmol) were stirred in THF (5.0 mL) under an argon atmosphere at 25 °C for 24 hours. Slow addition of K$_2$COT (30 mg, 0.17 mmol, in 2.0 mL of THF) to a violently stirred solution produced a cloudy yellow solution with a large amount of white precipitate formed in 30 minutes. The mixture was allowed to stir under an argon atmosphere at 25 °C for 48 hours to complete the reaction. The suspension was filtered, and the yellow filtrate was layered with 2.5 mL of anhydrous hexanes. The ampule was sealed under argon and stored at 5 °C. Yellow blocks were present in good yield after 5 days. Yield: 35 mg, 86%. ATR-IR: 678, 875, 888, 1030 cm^{-1}.

[ErKCa(COT)$_3$(THF)$_3$] (5-Er)

CaI$_2$ (16 mg, 0.055 mmol) and ErCl$_3$ (15 mg, 0.055 mmol) were stirred in THF (5.0 mL) under an argon atmosphere at 25 °C for 24 hours. Slow addition of K$_2$COT (30 mg, 0.17 mmol, in 2.0 mL of THF) to a violently stirred solution produced a cloudy yellow solution with a large amount of white precipitate formed in 30 minutes. The mixture was allowed to stir under an argon atmosphere at 25 °C for 48 hours to complete the reaction. The suspension was filtered, and the pink-orange filtrate was layered with 2.5 mL of anhydrous hexanes. The ampule was sealed under argon and stored at 5 °C. Yellow blocks were present in good yield after 5 days. Yield: 35 mg, 82%. ATR-IR: 679, 875, 889, 1030 cm^{-1}.

[TmKCa(COT)$_3$(THF)$_3$] (6-Tm)

CaI$_2$ (16 mg, 0.055 mmol) and TmCl$_3$ (15 mg, 0.055 mmol) were stirred in THF (5.0 mL) under an argon atmosphere at 25 °C for 24 hours. Slow addition of K$_2$COT (30 mg, 0.17 mmol, in 2.0 mL of THF) to a violently stirred solution produced a cloudy orange solution with a large amount of white precipitate formed in 30 minutes. The mixture was allowed to stir under an argon atmosphere at 25 °C for 48 hours to complete the reaction. The suspension was filtered, and the orange filtrate was layered with 2.5 mL of anhydrous hexanes. The ampule was sealed under argon and stored at 5 °C. Orange blocks were present in good yield after 6 days. Yield: 32 mg, 75%. ATR-IR: 679, 875, 889, 1030 cm^{-1}.

[YbKCa(COT)$_3$(THF)$_3$] (7-Yb)

CaI$_2$ (16 mg, 0.055 mmol) and YbCl$_3$ (15 mg, 0.055 mmol) were stirred in THF (5.0 mL) under an argon atmosphere at 25 °C for 24 hours. Slow addition of K$_2$COT (30 mg, 0.17 mmol, in 2.0 mL of THF) to a violently stirred solution produced a cloudy blue solution with a large amount of white precipitate in formed in 30 minutes. The mixture was allowed to stir under an argon atmosphere at 25 °C for 48 hours to complete the reaction. The suspension was filtered, and the blue filtrate was layered with 2.5 mL of anhydrous hexanes. The ampule was sealed under argon and stored at 5 °C. Blue blocks were present in good yield after 5 days. Yield: 35 mg, 81%. ATR-IR: 679, 875, 889, 1030 cm^{-1}.

II. ATR-IR Spectroscopic Investigation

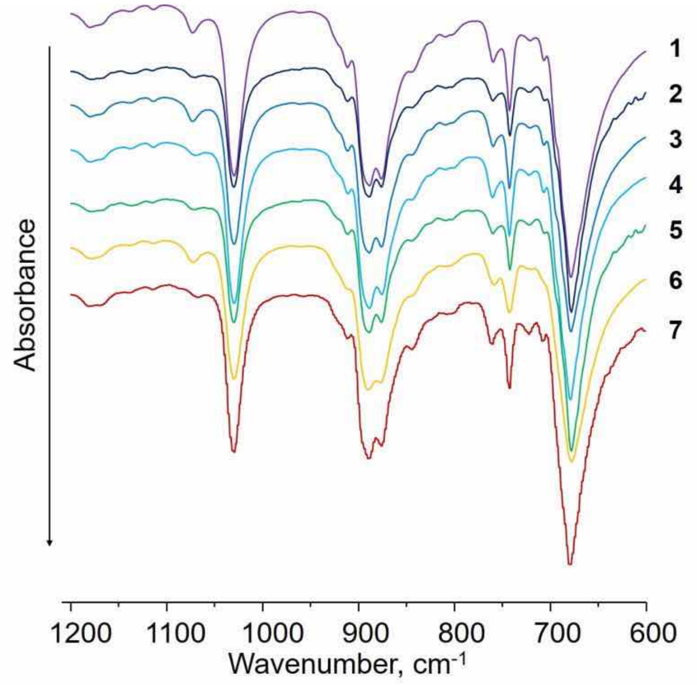

Fig. S1 ATR-IR spectra of **1–7**.

III. X-Ray Powder Diffraction and Le Bail Fit

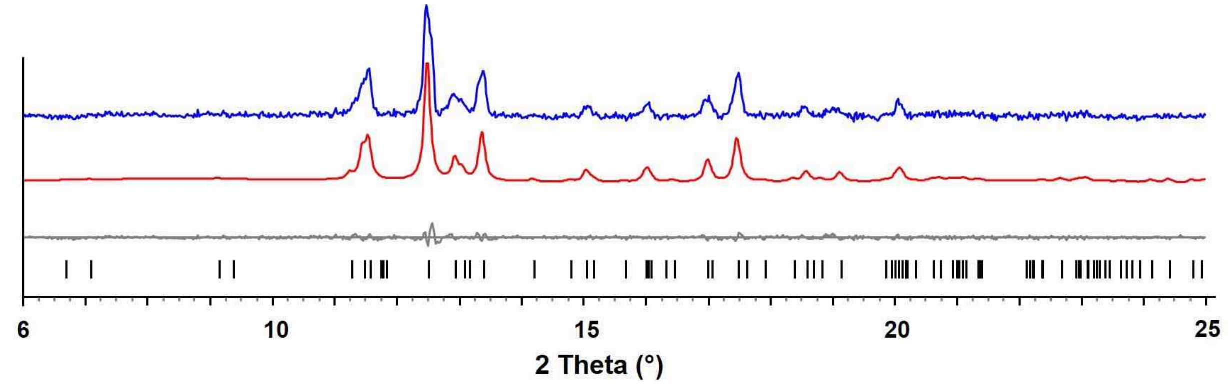

Fig. S2 X-ray powder diffraction pattern of **1-Gd** and Le Bail fit. The blue and red lines are experimental and calculated patterns, respectively. The grey line is the difference curve with theoretical positions shown at the bottom in black.

Table S1 Comparison of unit cell parameters for **1-Gd** from single crystal data and the Le Bail fit

1-Gd		
	Single crystal data (100 K)	Le Bail fit data (298 K)
Space Group	$P2_1/c$	
a (Å)	9.2772(3)	9.392(3)
b (Å)	13.9703(5)	14.079(2)
c (Å)	26.2056(9)	26.320(5)
α (°)	90	90
β (°)	90.079(1)	90.51(2)
γ (°)	90	90
V (Å^3)	3396.4(2)	3480.0(12)

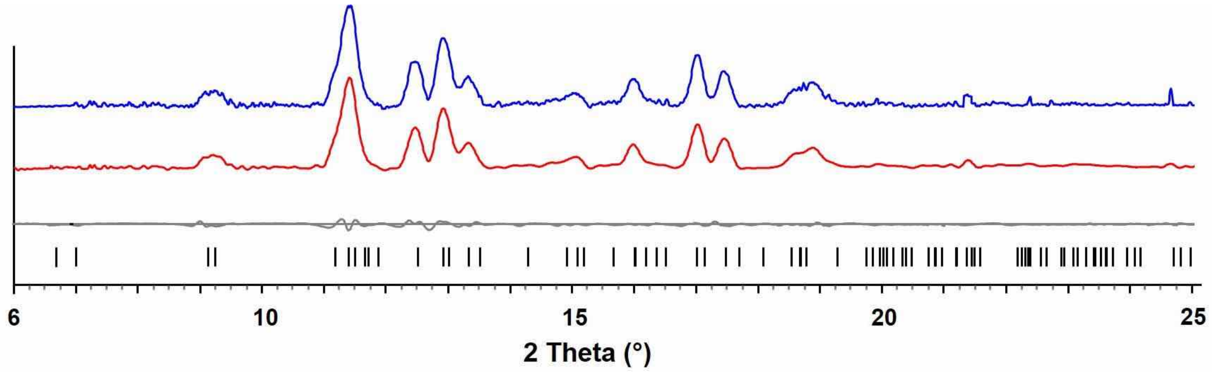

Fig. S3 X-ray powder diffraction pattern of **2-Tb** and Le Bail fit. The blue and red lines are experimental and calculated patterns, respectively. The grey line is the difference curve with theoretical positions shown at the bottom in black.

Table S2 Comparison of unit cell parameters for **2-Tb** from single crystal data and the Le Bail fit

2-Tb		
	Single crystal data (100 K)	Le Bail fit data (298 K)
Space Group	$P2_1/c$	
a (Å)	9.2738(6)	9.546(3)
b (Å)	13.9561(10)	14.271(9)
c (Å)	26.155(2)	25.571(9)
α (°)	90	90
β (°)	90.302(2)	90.76(2)
γ (°)	90	90
V (Å^3)	3385.1(4)	3619.7(2)

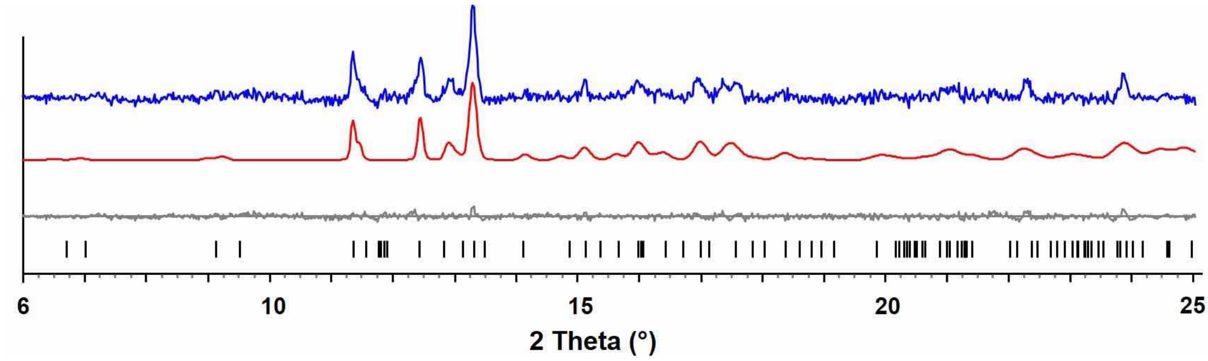

Fig. S4 X-ray powder diffraction pattern of **3-Dy** and Le Bail fit. The Blue and red lines are experimental and calculated patterns, respectively. The grey line is the difference curve with theoretical positions shown at the bottom in black.

Table S3 Comparison of unit cell parameters for **3-Dy** from single crystal data and the Le Bail fit

3-Dy		
	Single crystal data (100 K)	Le Bail fit data (298K)
Space Group	$P2_1/c$	
a (Å)	9.2628(5)	9.253(6)
b (Å)	13.9533(7)	14.235(4)
c (Å)	26.11417(13)	26.127(5)
α (°)	90	90
β (°)	90.377(2)	90.67(5)
γ (°)	90	90
V (Å^3)	3378.7(3)	3440.7(6)

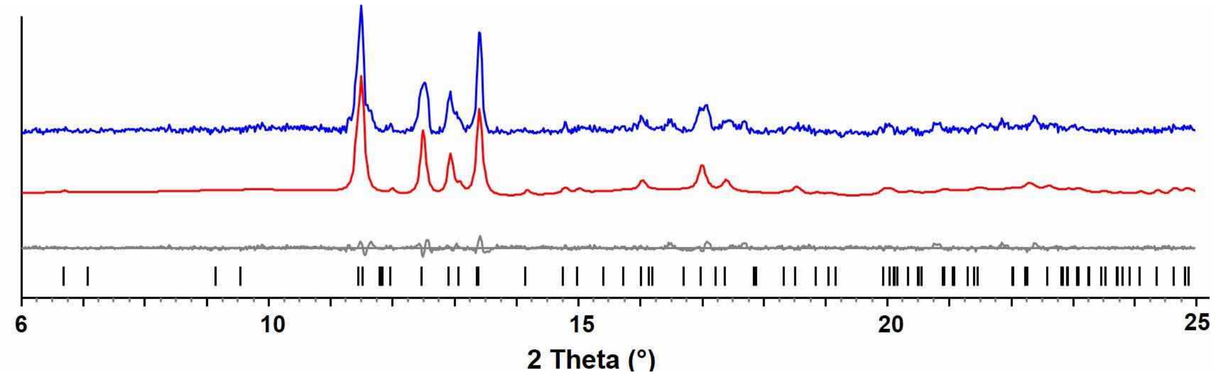

Fig. S5 X-ray powder diffraction pattern of **4-Ho** and Le Bail fit. The blue and red lines are experimental and calculated patterns, respectively. The grey line is the difference curve with theoretical positions shown at the bottom in black.

Table S4 Comparison of unit cell parameters for **4-Ho** from single crystal data and the Le Bail fit

4-Ho		
	Single crystal data (100 K)	Le Bail fit data (298 K)
Space Group	$P2_1/c$	
a (Å)	9.2613(3)	9.265(3)
b (Å)	13.9568(5)	14.190(3)
c (Å)	26.1226(10)	26.485(9)
α (°)	90	90
β (°)	90.566(2)	91.85(2)
γ (°)	90	90
V (Å^3)	3376.4(2)	3480.2(3)

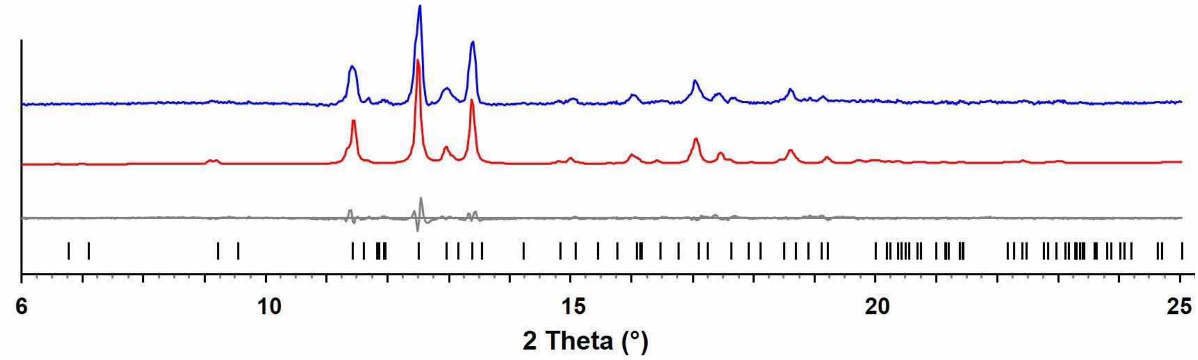

Fig. S6 X-ray powder diffraction pattern of **5-Er** and Le Bail fit. The blue and red lines are experimental and calculated patterns, respectively. The grey line is the difference curve with theoretical positions shown at the bottom in black.

Table S5 Comparison of unit cell parameters for **5-Er** from single crystal data and the Le Bail fit

5-Er		
	Single crystal data (100 K)	Le Bail fit data (298 K)
Space Group	$P2_1/c$	
a (Å)	9.2555(7)	9.251(6)
b (Å)	13.951(1)	14.150(1)
c (Å)	26.113(2)	26.092(6)
α (°)	90	90
β (°)	90.709(1)	91.12(5)
γ (°)	90	90
V (Å^3)	3371.6(4)	3415.0(5)

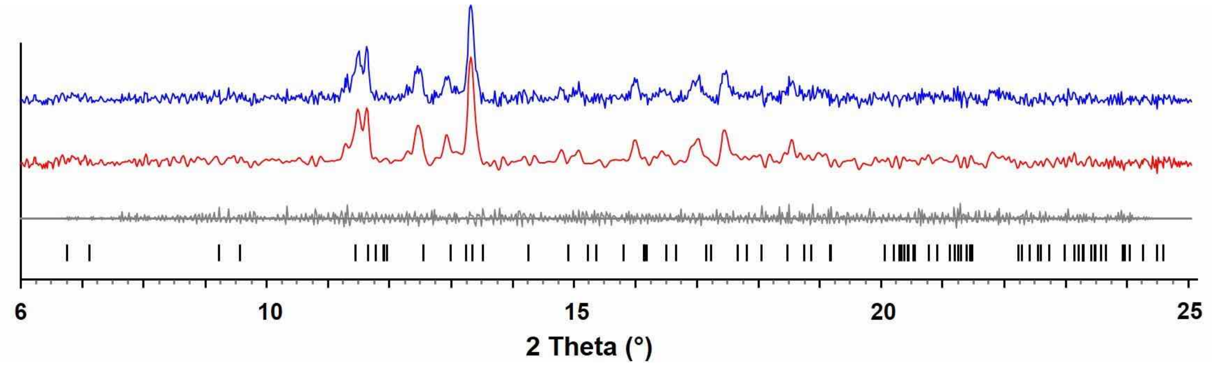

Fig. S7 X-ray powder diffraction pattern of **6-Tm** and Le Bail fit. The blue and red lines are experimental and calculated patterns, respectively. The grey line is the difference curve with theoretical positions shown at the bottom in black.

Table S6 Comparison of unit cell parameters for **6-Tm** from single crystal data and the Le Bail fit

6-Tm		
	Single crystal data (100 K)	Le Bail fit data (298 K)
Space Group	$P2_1/c$	
a (Å)	9.2730(7)	9.261(9)
b (Å)	13.9700(11)	14.11(4)
c (Å)	26.160(2)	26.21(2)
α (°)	90	90
β (°)	90.4780(10)	91.4(1)
γ (°)	90	90
V (Å^3)	3388.8(5)	3428.7(9)

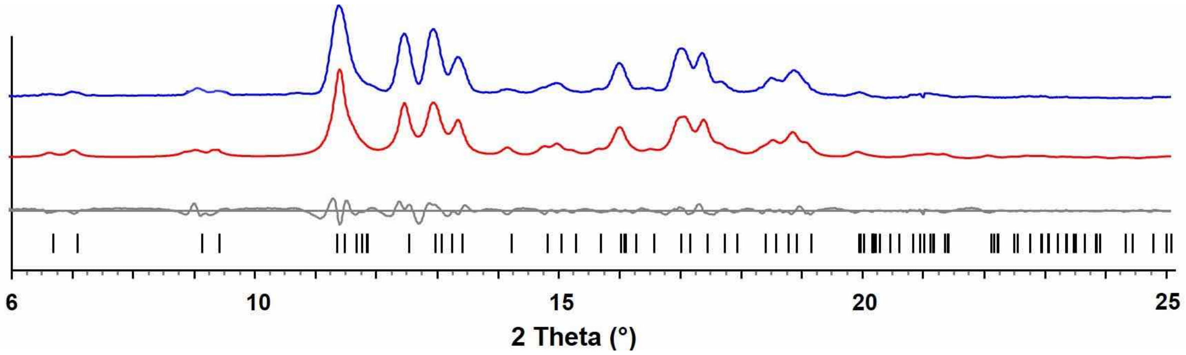

Fig. S8 X-ray powder diffraction pattern of **7-Yb** and Le Bail fit. The blue and red lines are experimental and calculated patterns, respectively. The grey line is the difference curve with theoretical positions shown at the bottom in black.

Table S7 Comparison of unit cell parameters for **7-Yb** from single crystal data and the Le Bail fit

7-Yb		
	Single crystal data (100 K)	Le Bail fit data (298 K)
Space Group	$P2_1/c$	
a (Å)	9.2730(7)	9.439(2)
b (Å)	13.9700(11)	14.203(3)
c (Å)	26.160(2)	26.553(7)
α (°)	90	90
β (°)	90.4780(10)	91.05(1)
γ (°)	90	90
V (Å^3)	3388.8(5)	3560.8(1)

IV. Crystal Structure Solution and Refinement Details

Data collections of **1**–**7** were performed on a Bruker D8 VENTURE X-ray diffractometer with PHOTON 100 CMOS shutterless mode detector equipped with a Mo-target X-ray tube ($\lambda = 0.71073$ Å) at $T = 100(2)$ K. Data reduction and integration were performed with the Bruker software package SAINT (version 8.38A).[3] Data were corrected for absorption effects using the empirical methods as implemented in SADABS (version 2016/2).[4] The structures were solved by SHELXT[5] and refined by full-matrix least-squares procedures using the Bruker SHELXTL (version 2016/6)[6] software package. All non-hydrogen atoms (including those in disordered parts) were refined anisotropically. The H atoms were also included at calculated positions and refined as riders, with $U_{\mathrm{iso}}(\mathrm{H}) = 1.2\ U_{\mathrm{eq}}(\mathrm{C})$. Crystallographic data for **1**–**7** and details of the data collection and structure refinement are listed in Table S8.

Table S8 Crystal data and structure refinement parameters for **1–7**

Compound	**1-Gd**	**2-Tb**	**3-Dy**	**4-Ho**
Empirical formula	$C_{36}H_{48}CaGdKO_3$	$C_{36}H_{48}CaTbKO_3$	$C_{36}H_{48}CaDyKO_3$	$C_{36}H_{48}CaHoKO_3$
Formula weight	765.17	766.84	770.42	772.85
Temperature (K)	100(2)	100(2)	100(2)	100(2)
Wavelength (Å)	0.71073	0.71073	0.71073	0.71073
Crystal system	Monoclinic	Monoclinic	Monoclinic	Monoclinic
Space group	$P2_1/c$	$P2_1/c$	$P2_1/c$	$P2_1/c$
a (Å)	9.2772(3)	9.2738(6)	9.2628(5)	9.2613(3)
b (Å)	13.9703(5)	13.9561(10)	13.9533(7)	13.9568(5)
c (Å)	26.2056(9)	26.1550(18)	26.1417(13)	26.1226(10)
α (°)	90.00	90.00	90.00	90.00
β (°)	90.0790(10)	90.302(2)	90.377(2)	90.566(2)
γ (°)	90.00	90.00	90.00	90.00
V (Å^3)	3396.4(2)	3385.1(4)	3378.7(3)	3376.4(2)
Z	4	4	4	4
ρ_{calcd} (g·cm^{-3})	1.496	1.505	1.515	1.520
μ (mm^{-1})	2.259	2.397	2.520	2.652
F(000)	1564	1568	1572	1576
Crystal size (mm)	0.03×0.17×0.52	0.10×0.15×0.48	0.04×0.15×0.39	0.05×0.07×0.21
θ range for data collection (°)	2.75-33.79	3.02-43.20	2.75-25.05	2.75-30.57
Reflections collected	95537	191623	74320	135796
Independent reflections	13580 [R_{int} = 0.0591]	25203 [R_{int} = 0.0754]	5954 [R_{int} = 0.0885]	10339 [R_{int} = 0.0630]
Transmission factors (min/max)	0.5352/0.7467	0.7320/0.8456	0.7730/0.8653	0.7940/0.8992
Data/restraints/params.	13580/0/379	25203/0/379	5954/849/373	10339/0/379
$R1$,[a] $wR2$[b] ($I > 2\sigma(I)$)	0.0457, 0.0617	0.0424, 0.0933	0.0584, 0.1247	0.0333, 0.0545
$R1$,[a] $wR2$[b] (all data)	0.0710, 0.0673	0.0541, 0.0980	0.0727, 0.1313	0.0477, 0.0578
Quality-of-fit[c]	1.094	1.108	1.141	1.090

Compound	**5-Er**	**6-Tm**	**7-Yb**
Empirical formula	$C_{36}H_{48}CaErKO_3$	$C_{36}H_{48}CaTmKO_3$	$C_{36}H_{48}CaYbKO_3$
Formula weight	775.18	776.85	780.96
Temperature (K)	100(2)	100(2)	100(2)
Wavelength (Å)	0.71073	0.71073	0.71073
Crystal system	Monoclinic	Monoclinic	Monoclinic
Space group	$P2_1/c$	$P2_1/c$	$P2_1/c$
a (Å)	9.2555(7)	9.2649(8)	9.2602(7)
b (Å)	13.9514(11)	13.9648(11)	13.9561(10)
c (Å)	26.113(2)	26.111(2)	26.1046(19)
α (°)	90.00	90.00	90.00
β (°)	90.7090(10)	90.8583(15)	90.935(2)
γ (°)	90.00	90.00	90.00
V (Å^3)	3371.6(4)	3377.9(5)	3373.2(4)
Z	4	4	4
ρ_{calcd} (g·cm^{-3})	1.527	1.528	1.538
μ (mm^{-1})	2.798	2.935	3.081
F(000)	1580	1584	2084
Crystal size (mm)	0.05×0.08×0.24	0.03×0.17×0.32	0.04×0.15×0.52
θ range for data collection (°)	2.75-35.08	2.76-37.87	2.74-37.10
Reflections collected	197098	108685	88786
Independent reflections	14885 [R_{int} = 0.0712]	17902 [R_{int} = 0.0415]	16802 [R_{int} = 0.0428]
Transmission factors (min/max)	0.6938/0.7569	0.4232/0.7474	0.6648/0.7896
Data/restraints/params.	14885/0/379	17902/0/379	16802/0/379
$R1$,[a] $wR2$[b] ($I > 2\sigma(I)$)	0.0339, 0.0508	0.0385, 0.0707	0.0363, 0.0493
$R1$,[a] $wR2$[b] (all data)	0.0495, 0.0542	0.0550, 0.0753	0.0564, 0.0530
Quality-of-fit[c]	1.094	1.129	1.073

[a] $R_1 = \Sigma||F_o|-|F_c||/\Sigma|F_o|$. [b] $wR_2 = [\Sigma[w(F_o^2-F_c^2)^2]/\Sigma[w(F_o^2)^2]]$.

[c] Quality-of-fit $S = [\Sigma[w(F_o^2-F_c^2)^2]/(N_{\text{obs}}-N_{\text{params}})]^{½}$, based on all data.

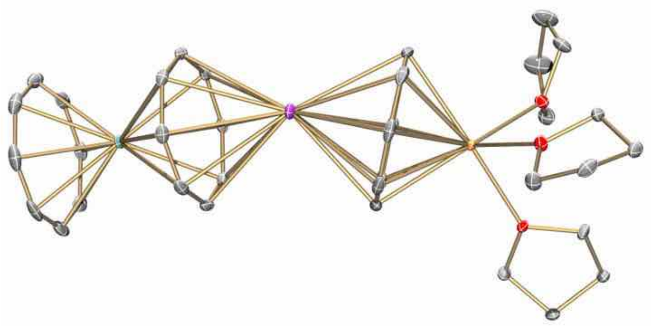

Fig. S9 ORTEP drawing of **1-Gd**, drawn with thermal ellipsoids at the 40% probability level. All hydrogen atoms are removed for clarity. The color scheme used: C grey, O red, K dark orchid, Ca orange, Gd green copper.

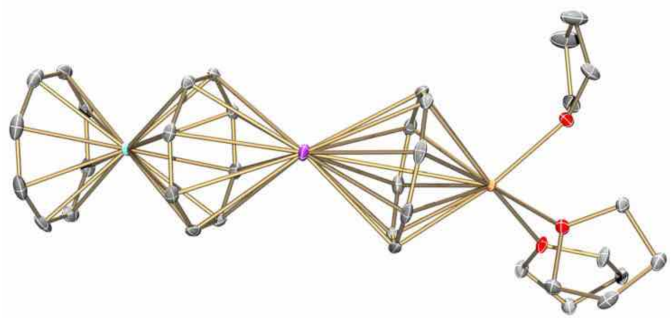

Fig. S10 ORTEP drawing of **2-Tb**, drawn with thermal ellipsoids at the 40% probability level. All hydrogen atoms are removed for clarity. The color scheme used: C grey, O red, K dark orchid, Ca orange, Tb medium turquoise.

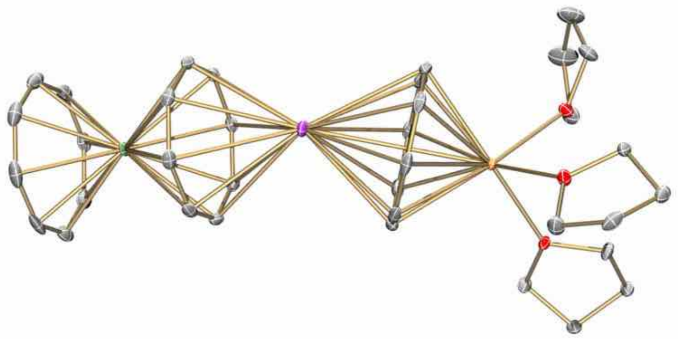

Fig. S11 ORTEP drawing of **3-Dy**, drawn with thermal ellipsoids at the 40% probability level. All hydrogen atoms are removed for clarity. The color scheme used: C grey, O red, K dark orchid, Ca orange, Dy medium sea green.

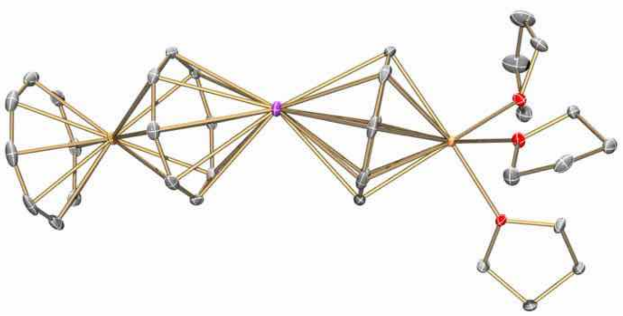

Fig. S12 ORTEP drawing of **4-Ho**, drawn with thermal ellipsoids at the 40% probability level. All hydrogen atoms are removed for clarity. The color scheme used: C grey, O red, K dark orchid, Ca orange, Ho sienna.

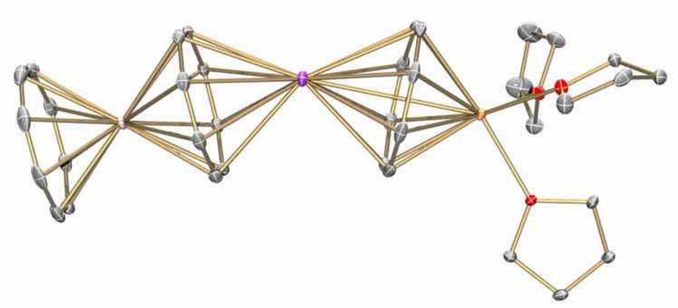

Fig. S13 ORTEP drawing of **5-Er**, drawn with thermal ellipsoids at the 40% probability level. All hydrogen atoms are removed for clarity. The color scheme used: C grey, O red, K dark orchid, Ca orange, Er pink.

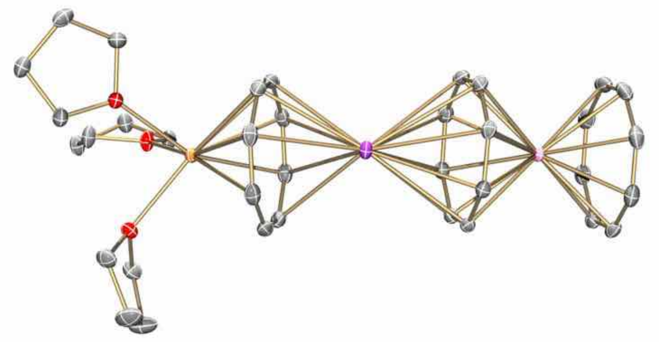

Fig. S14 ORTEP drawing of **6-Tm**, drawn with thermal ellipsoids at the 40% probability level. All hydrogen atoms are removed for clarity. The color scheme used: C grey, O red, K dark orchid, Ca orange, Tm medium violet.

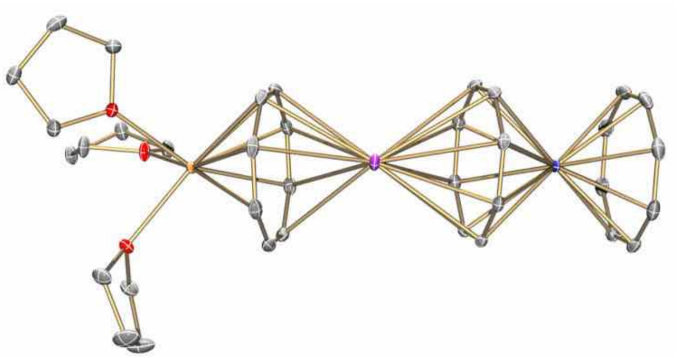

Fig. S15 ORTEP drawing of **7-Yb**, drawn with thermal ellipsoids at the 40% probability level. All hydrogen atoms are removed for clarity. The color scheme used: C grey, O red, K dark orchid, Ca orange, Yb navy blue.

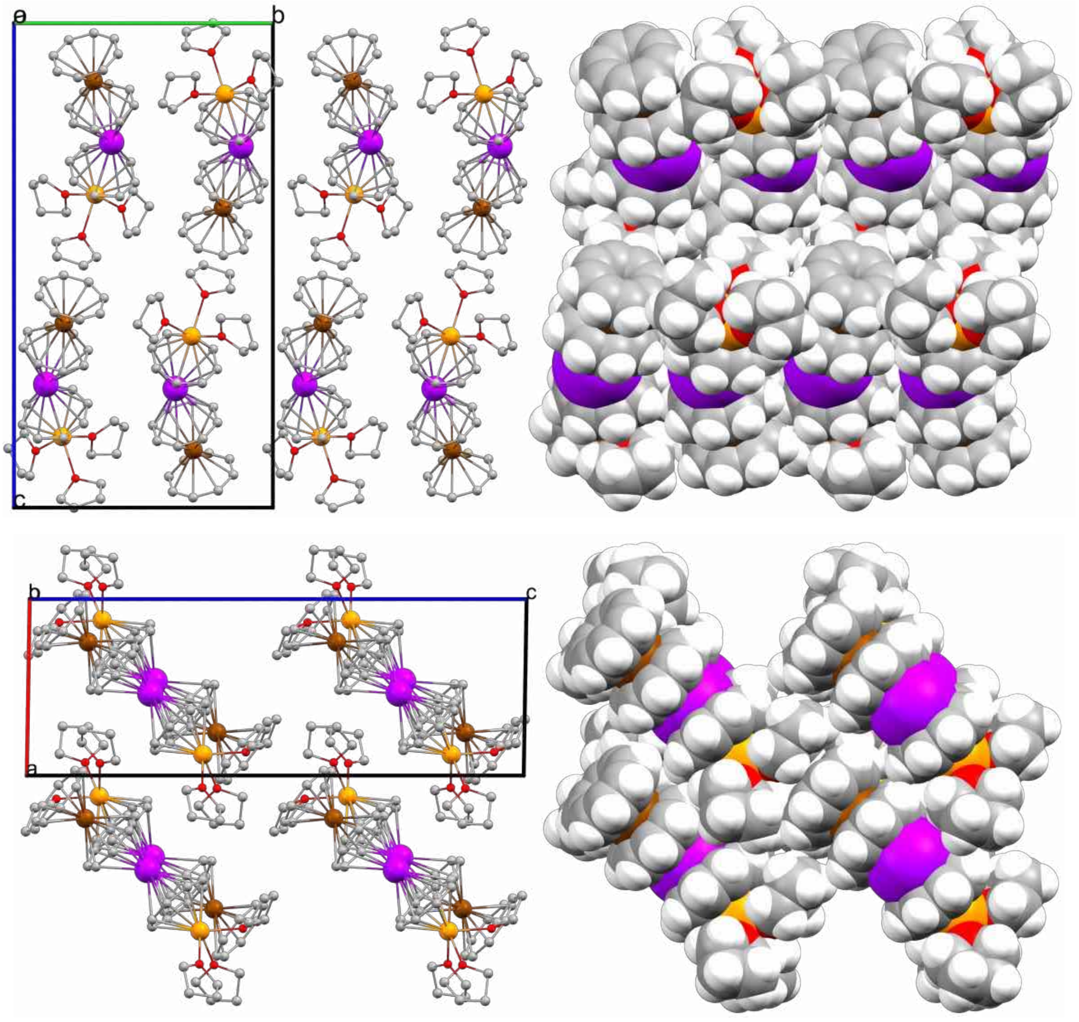

Fig. S16 Solid-state packing of **1**–**7**, ball-and-stick (no H-atoms) and space-filling models.

Table S9 Selected bond length distances (Å) in **1**–**7** along with a labeling scheme

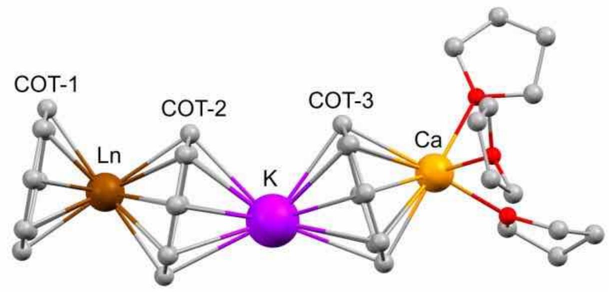

	1-Gd	**2-Tb**	**3-Dy**	**4-Ho**	**5-Er**	**6-Tm**	**7-Yb**
Ln–$C_{COT1, avg}$	2.653(3)	2.640(2)	2.623(8)	2.615(3)	2.606(2)	2.599(2)	2.593(2)
Ln to $centroid_{COT1}$	1.913(3)	1.891(2)	1.874(8)	1.859(3)	1.846(2)	1.832(2)	1.827(2)
Ln–$C_{COT2, avg}$	2.691(3)	2.677(2)	2.662(8)	2.651(3)	2.644(2)	2.637(2)	2.614(2)
Ln to $centroid_{COT2}$	1.961(3)	1.939(2)	1.923(8)	1.907(3)	1.896(2)	1.881(2)	1.871(2)
K–$C_{COT2, avg}$	3.089(3)	3.089(2)	3.088(8)	3.086(3)	3.086(2)	3.089(2)	3.089(2)
K to $centroid_{COT2}$	2.479(3)	2.476(2)	2.478(8)	2.476(3)	2.475(2)	2.476(2)	2.478(2)
K–$C_{COT3, avg}$	3.032(3)	3.032(2)	3.030(8)	3.030(3)	3.031(2)	3.034(2)	3.032(2)
K to $centroid_{COT3}$	2.409(3)	2.407(2)	2.408(8)	2.407(3)	2.408(2)	2.409(2)	2.407(2)
Ca–$C_{COT3, avg}$	2.655(2)	2.658(2)	2.653(8)	2.656(2)	2.656(2)	2.658(2)	2.657(2)
Ca to $centroid_{COT3}$	1.915(2)	1.914(2)	1.912(8)	1.914(2)	1.913(2)	1.916(2)	1.913(2)
Ca–$O_{THF, avg}$	2.383(2)	2.383(1)	2.382(5)	2.382(2)	2.381(2)	2.384(2)	2.383(1)

Table S10 Selected dihedral angles (°) in **1–7**

	1-Gd	**2-Tb**	**3-Dy**	**4-Ho**	**5-Er**	**6-Tm**	**7-Yb**
COT1/COT2	0.77(9)	0.85(6)	0.90(3)	0.84(9)	0.81(7)	0.83(6)	0.89(6)
COT2/COT3	27.61(9)	27.45(6)	27.60(3)	27.47(9)	27.41(7)	27.33(6)	27.35(6)

Table S11 C–H···π interactions (Å) in **1–7** along with a labeling scheme

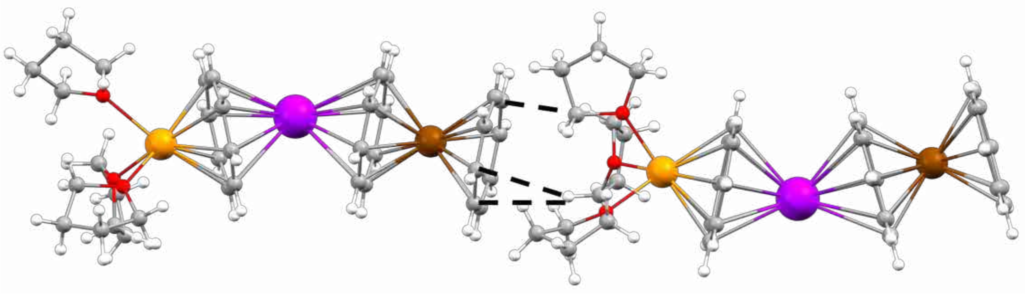

	1-Gd	**2-Tb**	**3-Dy**	**4-Ho**	**5-Er**	**6-Tm**	**7-Yb**
C–H···π interaction	2.721(2)–2.747(2)	2.708(1)–2.732(1)	2.708(5)–2.751(5)	2.702(2)–2.729(2)	2.693(2)–2.731(2)	2.697(3)–2.725(3)	2.692(1)–2.728(1)

Table S12 Selected M–M distances (Å) in **1–7**

	1-Gd	**2-Tb**	**3-Dy**	**4-Ho**	**5-Er**	**6-Tm**	**7-Yb**
Intermolecular Ln–Ln	9.277(2)	9.274(2)	9.263(2)	9.261(2)	9.255(2)	9.265(2)	9.260(2)
Intramolecular Ln–K	4.440(2)	4.414(2)	4.400(2)	4.383(2)	4.369(2)	4.356(2)	4.348(2)
Intramolecular Ca–K	4.323(2)	4.320(2)	4.319(2)	4.321(2)	4.320(2)	4.323(2)	4.319(2)

V. Magnetic Properties

Magnetic susceptibility measurements were performed on a Quantum Design SQUID MPMS-XL magnetometer and PPMS-II susceptometer housed at the Centre de Recherche Paul Pascal at temperatures between 1.8 and 400 K and *dc* magnetic fields ranging from -7 to +7 T. The *ac* magnetic susceptibility measurements were performed in an oscillating *ac* field of 1 to 6 Oe with frequencies between 10 and 10000 Hz in zero *dc*-field. The measurements were carried out on polycrystalline samples (3.3 for **1-Gd**, 4.5 mg for **2-Tb**, 3.1, 6.8, 4.9 mg for **3-Dy**, 2.7 mg for **4-Ho**, 10.5 mg for **5-Er** and 6.0 mg for **6-Tm**) suspended in mineral oil (typically 5-20 mg) and introduced in a sealed polyethene bag (3 × 0.5 × 0.02 cm; typically, 20-40 mg) in a glovebox a controlled atmosphere of nitrogen or argon. Prior to the experiments, the field-dependent magnetisation was measured at 100 K on each sample in order to detect the presence of any bulk ferromagnetic impurities. As expected for paramagnetic or diamagnetic materials, a perfectly linear dependence of the magnetisation that extrapolates to zero at zero *dc* field was systematically observed; the samples appeared to be free of any ferromagnetic impurities. The magnetic susceptibilities were corrected for the sample holder, the mineral oil and the intrinsic diamagnetic contributions.

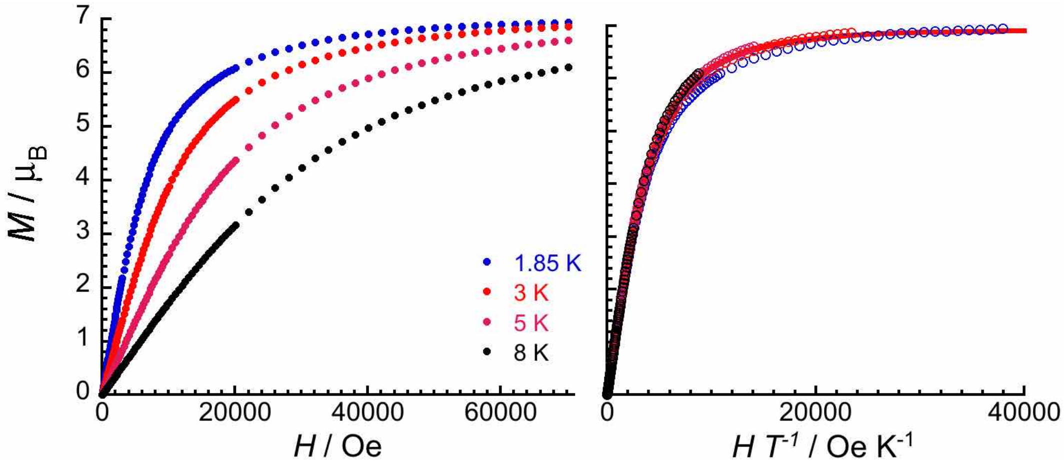

Fig. S17 Field dependence of the magnetisation for **1-Gd** at low temperatures between 1.85 and 8 K with applied magnetic field from 0 to 7 T. The magnetization data are shown as a *M* versus *H* plot on the left and as a *M* versus *H*/*T* plot on the right (field sweeping rates: 80 Oe/min between 0 and 0.1 T, 170 Oe/min between 0.1 and 0.3 T, 400 Oe/min between 0.3 and 1 T, 830 Oe/min between 1 and 2 T, 2800 Oe/min between 2 and 7 T). At 1.85 K and 7 T, the magnetization reaches a value of 6.94 μ_B. The solid red line is the best fit of the experimental *M* versus *H*/*T* data to the S = 7/2 Brillouin function with *g* = 1.98(3).

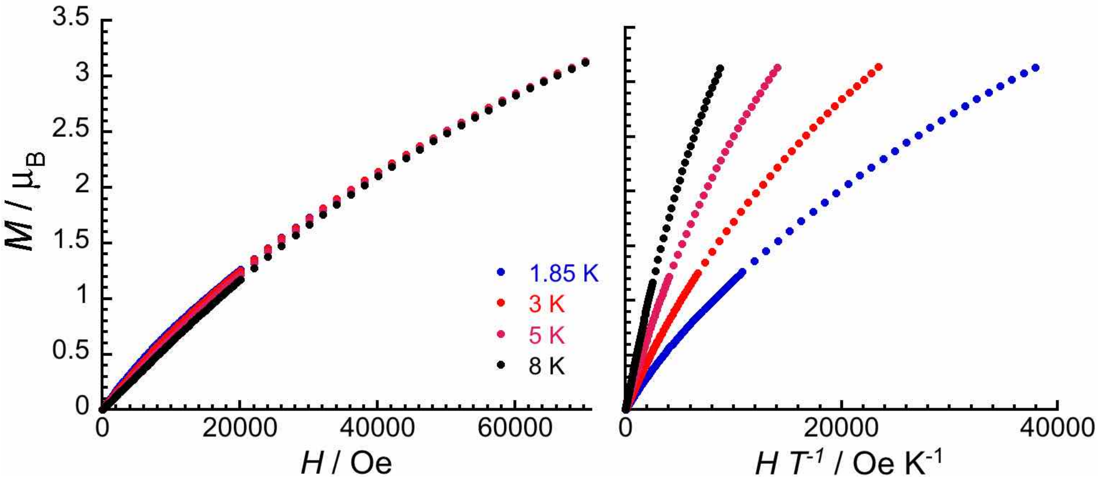

Fig. S18 Field dependence of the magnetisation for **2-Tb** at low temperatures between 1.85 and 8 K with applied magnetic field from 0 to 7 T. The magnetization data are shown as a *M* versus *H* plot on the left and as a *M* versus *H*/*T* plot on the right (field sweeping rates: 80 Oe/min between 0 and 0.1 T, 170 Oe/min between 0.1 and 0.3 T, 400 Oe/min between 0.3 and 1 T, 830 Oe/min between 1 and 2 T, 2800 Oe/min between 2 and 7 T). At 1.85 K and 7 T, the magnetization reaches a value of 3.13 μ_B.

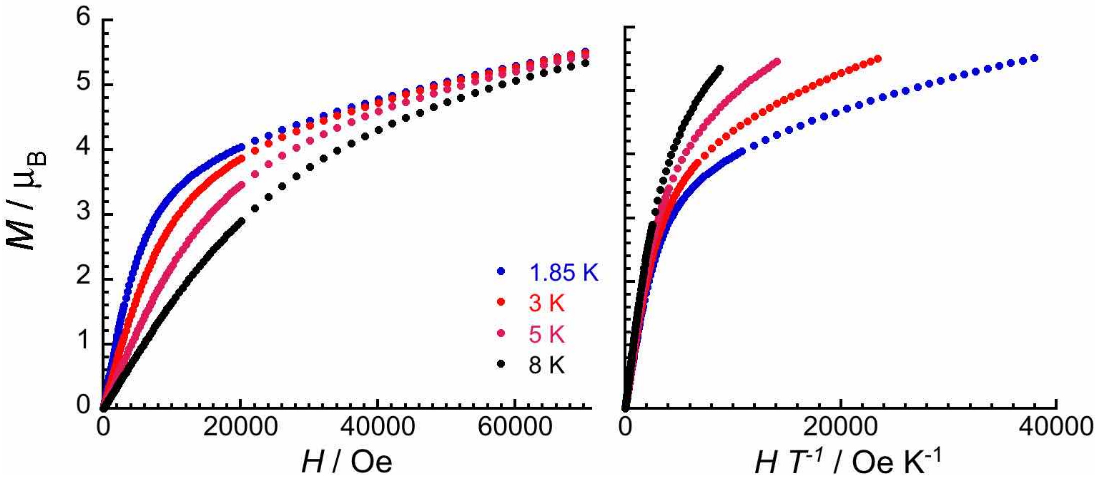

Fig. S19 Field dependence of the magnetisation for **3-Dy** at low temperatures between 1.85 and 8 K with applied magnetic field from 0 to 7 T. The magnetization data are shown as a *M* versus *H* plot on the left and as a *M* versus *H*/*T* plot on the right (field sweeping rates: 80 Oe/min between 0 and 0.1 T, 170 Oe/min between 0.1 and 0.3 T, 400 Oe/min between 0.3 and 1 T, 830 Oe/min between 1 and 2 T, 2800 Oe/min between 2 and 7 T). At 1.85 K and 7 T, the magnetization reaches a value of 5.52 μ_B.

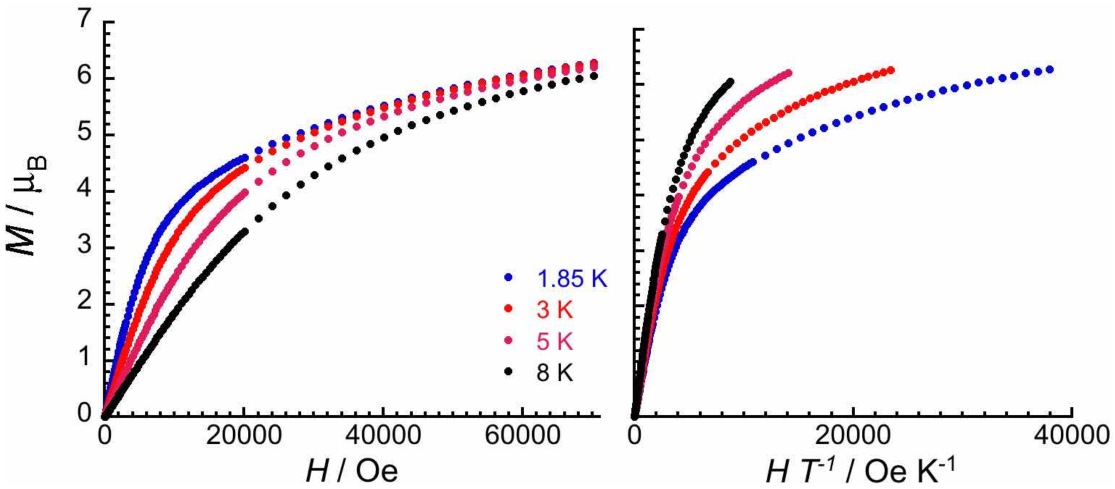

Fig. S20 Field dependence of the magnetisation for **4-Ho** at low temperatures between 1.85 and 8 K with applied magnetic field from 0 to 7 T. The magnetization data are shown as a *M* versus *H* plot on the left and as a *M* versus *H*/*T* plot on the right (field sweeping rates: 80 Oe/min between 0 and 0.1 T, 170 Oe/min between 0.1 and 0.3 T, 400 Oe/min between 0.3 and 1 T, 830 Oe/min between 1 and 2 T, 2800 Oe/min between 2 and 7 T). At 1.85 K and 7 T, the magnetization reaches a value of 6.28 μ_B.

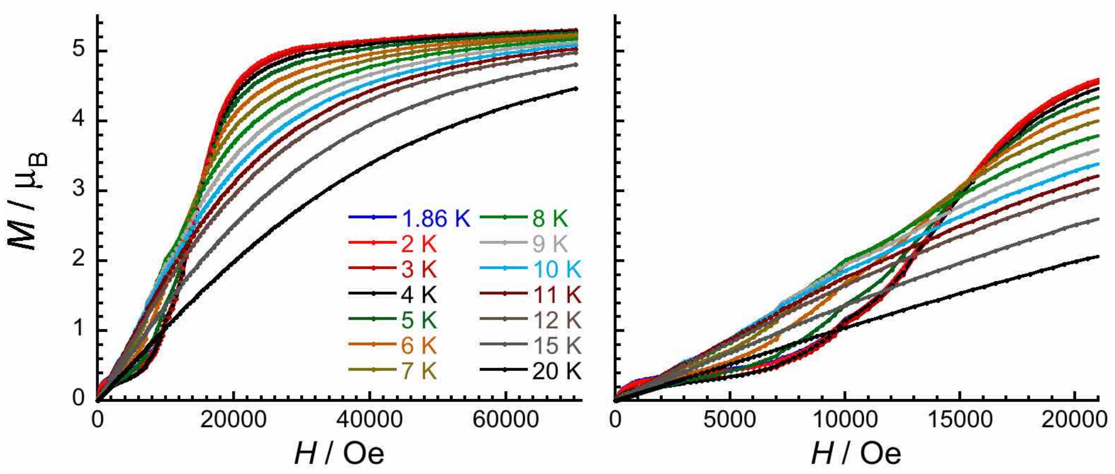

Fig. S21 Field dependence of the magnetisation for **5-Er** at low temperatures between 1.85 and 8 K with applied magnetic field from 0 to 7 T (after a zero-field cooling from 20 K). The *M* versus *H* data are shown on full scale from 0 to 7 T on the left and between 0 and 2.1 T on the right (field sweeping rates: 80 Oe/min between 0 and 0.1 T, 170 Oe/min between 0.1 and 0.3 T, 400 Oe/min between 0.3 and 1 T, 830 Oe/min between 1 and 3 T, 2800 Oe/min between 3 and 7 T). At 1.85 K and 7 T, the magnetization reaches a value of 5.29 μ_B.

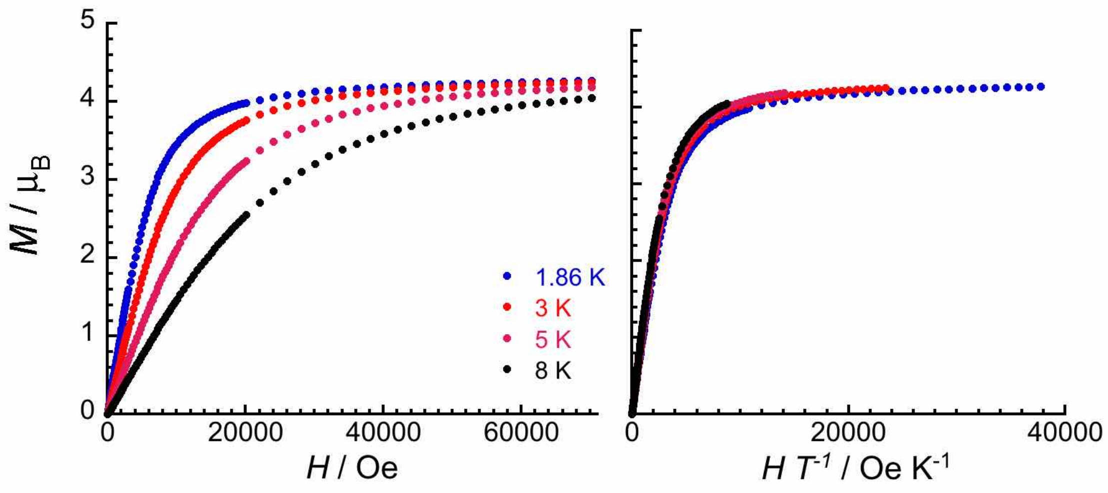

Fig. S22 Field dependence of the magnetisation for **6-Tm** at low temperatures between 1.85 and 8 K with applied magnetic field from 0 to 7 T. The magnetization data are shown as a *M* versus *H* plot on the left and as a *M* versus *H*/*T* plot on the right (field sweeping rates: 80 Oe/min between 0 and 0.1 T, 170 Oe/min between 0.1 and 0.3 T, 400 Oe/min between 0.3 and 1 T, 830 Oe/min between 1 and 2 T, 2800 Oe/min between 2 and 7 T). At 1.85 K and 7 T, the magnetization reaches a value of 4.27 μ_B.

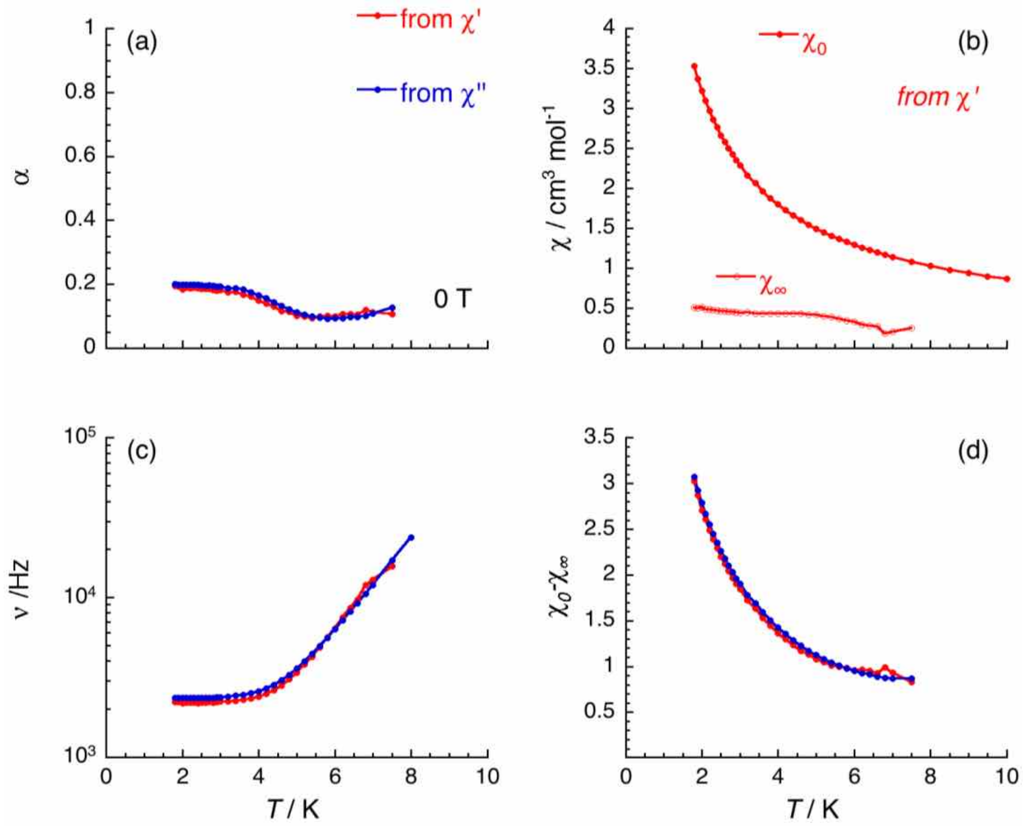

Fig. S23 Temperature dependence of the parameters α, v, χ_0, χ_∞ and χ_0-χ_∞, between 1.85 and 8 K in zero-dc field deduced from the generalised Debye fit of the frequency dependence of the real (χ') and imaginary (χ'') components of the ac susceptibility shown in Fig. 7 (main text), for **3-Dy**.

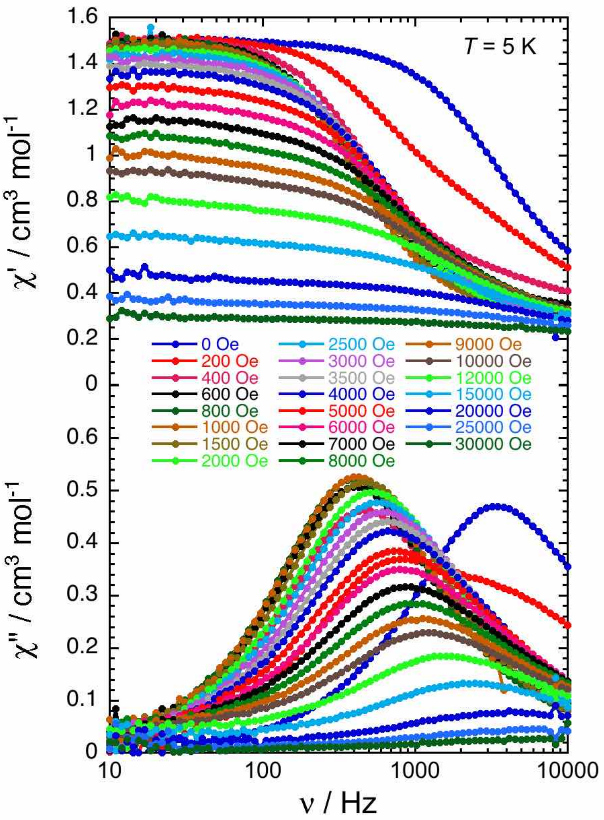

Fig. S24 ac frequency dependences (between 0.1 and 10000 Hz) of the real (χ', top) and imaginary (χ'', bottom) parts of the ac susceptibility for **3-Dy** at 5 K and under an applied dc field varying between 0 and 3 T. The solid lines are guides for the eyes.

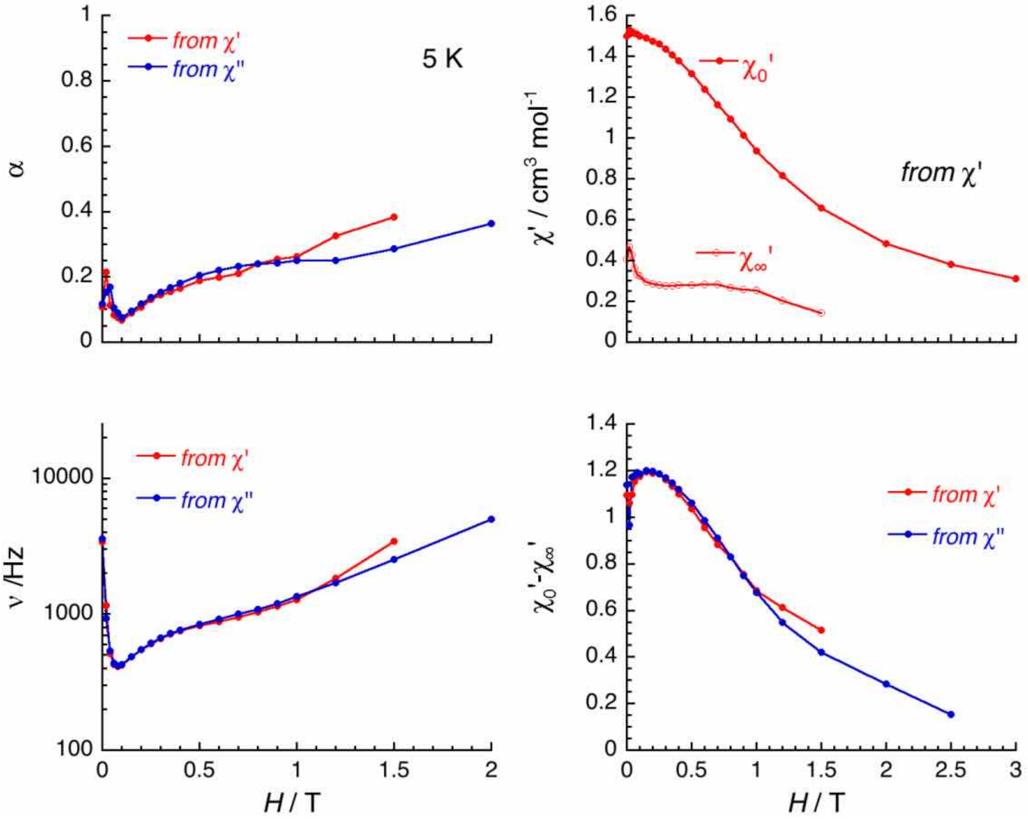

Fig. S25 Field dependence of the parameters *α*, *v*, χ_0, χ_∞ and χ_0-χ_∞, between 0 and 2 T at 5 K deduced from the generalised Debye fit of the frequency dependence of the real (χ') and imaginary (χ'') components of the ac susceptibility shown in the above Fig. S24, for **3-Dy**.

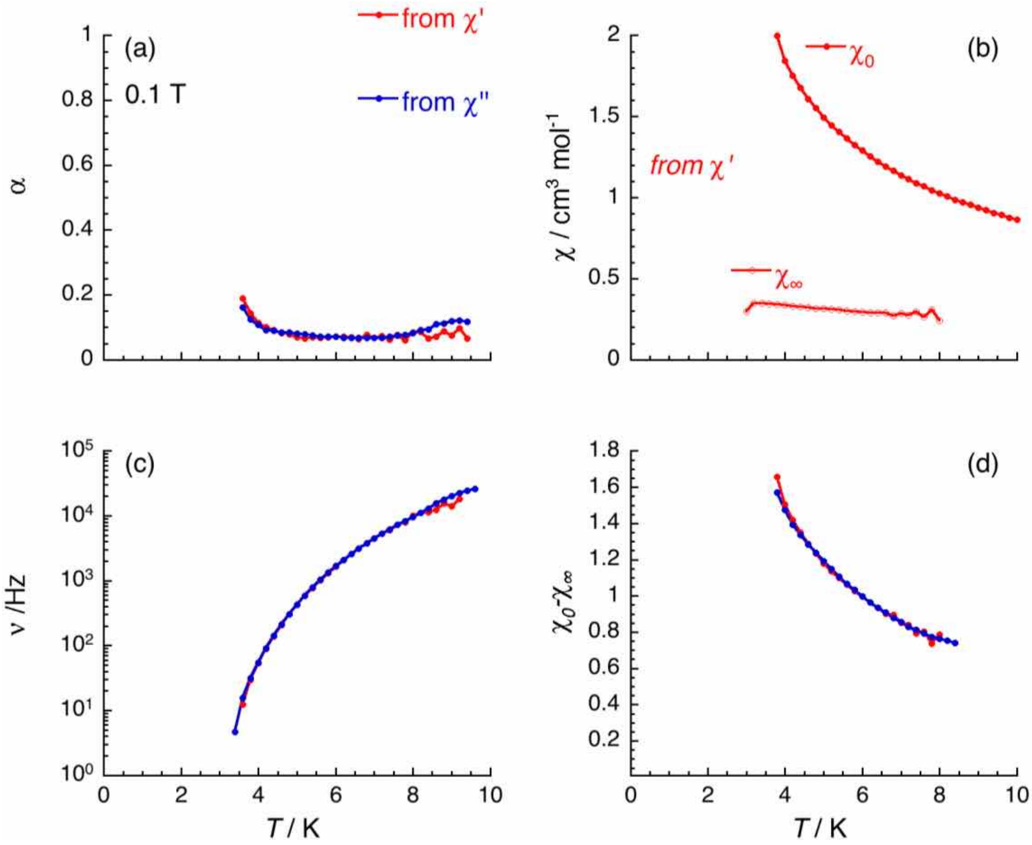

Fig. S26 Temperature dependence of the parameters α, ν, χ_0, χ_∞ and χ_0-χ_∞, between 3.4 and 9.2 K under an applied dc field of 0.1 T, deduced from the generalised Debye fit of the frequency dependence of the real (χ') and imaginary (χ'') components of the ac susceptibility shown in Fig. 8 (main text), for **3-Dy**.

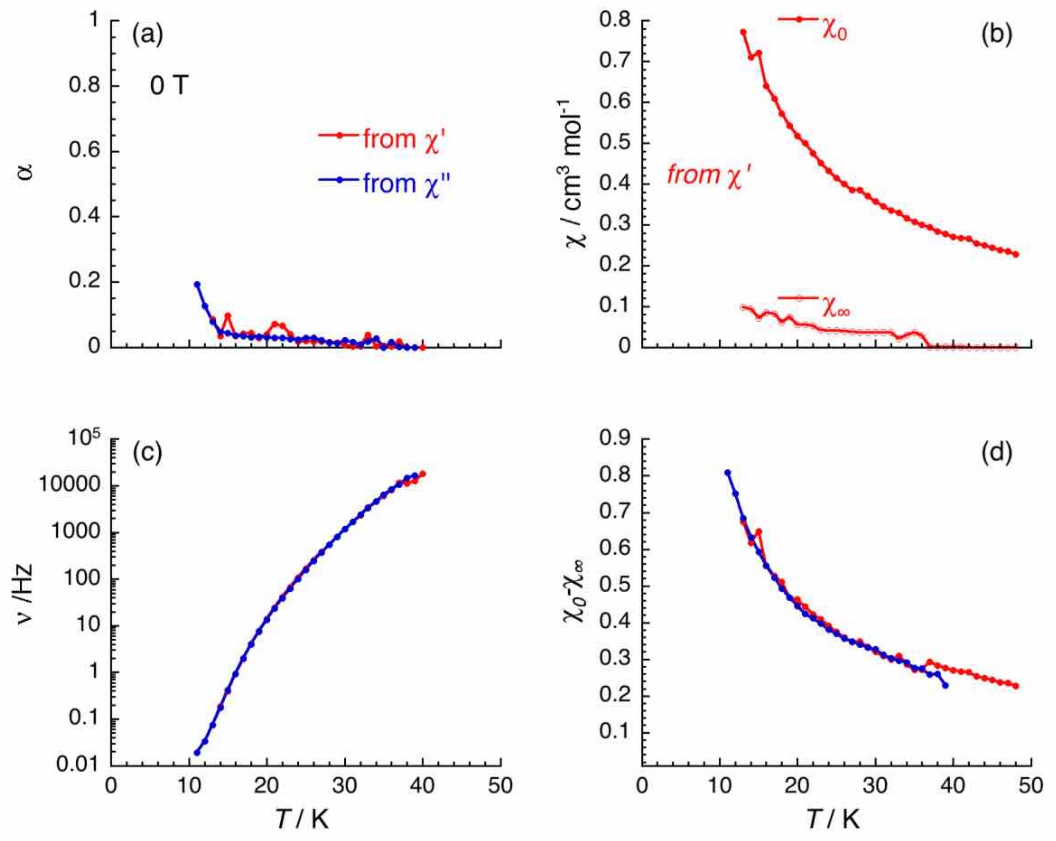

Fig. S27 Temperature dependence of the parameters α, v, χ_0, χ_∞ and χ_0-χ_∞, between 1.85 and 8 K in zero-dc field deduced from the generalised Debye fit of the frequency dependence of the real (χ') and imaginary (χ'') components of the ac susceptibility shown in Fig. 10 (main text), for **5-Er**.

The relaxation rate, τ^{-1}, of a given system can thus be summarized by the following equations:

$$\tau^{-1} = \tau_{Raman}^{-1} + \tau_{Direct}^{-1} + \tau_{Orbach}^{-1} + \tau_{QTM}^{-1} \tag{1}$$

$$\tau^{-1} = C\frac{1+C_1H^2}{1+C_2H^2}T^n + ATH^4 + \tau_0^{-1}\exp\left(-\frac{\Delta\left(1-\frac{H}{H_0}\right)^m}{k_BT}\right) + \frac{B_1}{1+B_2H^2} \tag{2}$$

Equation 2 shows that these four processes have their own temperature (T) and field (H) dependence, which rely on a eleven parameters (A, n, B_1, B_2, C, C_1, C_2, Δ, τ_0, m and H_0; with for the Orbach-like relaxation, Δ being the energy barrier at zero applied field, H_0 the reversal field at zero temperature, τ_0 the attempt relaxation time and m a constant of the order of the unity usually between 1.5 and 2).

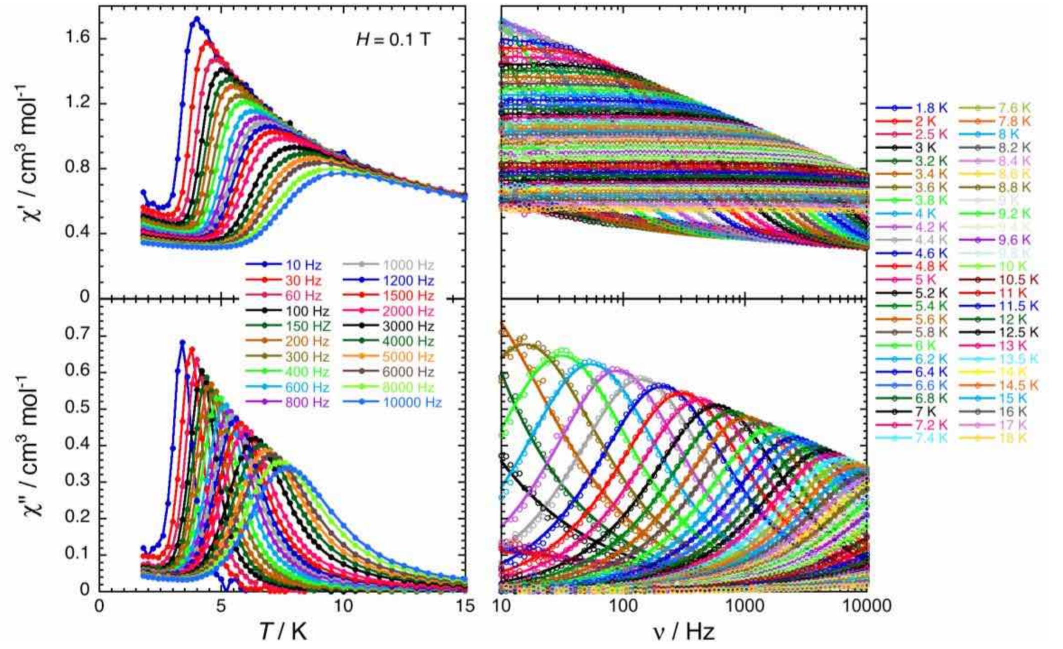

Fig. S28 In-phase (top) and out-of-phase (bottom) components of the molar ac magnetic susceptibility of **3-Dy** measured as a function of temperature at different frequencies (left) and as a function of frequency at different temperatures (right) in 0.1 T dc-field. The solid lines on the left plots are guides for the eyes. The solid lines on the right plots are the generalized Debye fits[7, 8] of the experimental ac susceptibility data (open dots).

With an eleven-parameter model, it is absolutely unrealistic to fit the experimental data without falling in an overparametrization of the experimental data. Therefore, some experimental observations must be used to simplify the relaxation model and eliminate some contribution(s) in the equation 1. Indeed, the τ versus H, shown on the left part of Fig. S29, is very informative. The relaxation time of **3-Dy** shows a very slow decrease above 0.1 T incompatible with a H^{-4} or H^{-2} variation expected for Direct or Raman ($C_2 < C_1$) processes. As a consequence, and based on equation 2, this field behavior (> 0.1 T) could only be potentially reproduced by an Orbach-like relaxation. At low fields below 0.05 T, the relaxation time is compatible with an H^{2} variation expected for QTM or Raman (with $C_2 > C_1$) mechanisms. Therefore, in a first approximation, two simple models involving (i) Raman and Orbach-like, or (ii) QTM and Orbach-like relaxation processes can be considered to fit simultaneously all the experimental data. Indeed, both models are able to reproduce the τ versus H and τ versus T variations in a similar good agreement that is undistinguishable in Fig. S29. Nevertheless, the low value of n (smaller than 1), the lower numbers of adjustable parameters (5 versus 7; with m fixed to 2) and the much larger error bar on the obtained parameters (suggesting overparametrization) favor the second model implying QTM and Orbach-like relaxations. The best set of parameters involving the two last terms of equation 2 are $B_1 = 1.4(1)\ 10^4\ \mathrm{s}^{-1}$ (or $\tau_{\mathrm{QTM}} = B_1^{-1} \approx 7\ 10^{-7}$ s), $B_2 = 5(1)\ 10^4\ \mathrm{T}^{-2}$, $\tau_0 = 8(2)\times10^{-8}$ s, $\Delta/k_{\mathrm{B}} = 43(1)$ K ($\Delta_{\mathrm{eff}}/k_{\mathrm{B}} = 37(3)$ K in zero-dc field due likely to resonant QTM that shortcuts the total energy barrier),[9] and $H_0 = 13(2)$ T. It is important to note that the origin of the Orbach-like relaxation with an energy gap of about 40 K is not obvious for a mononuclear Dy complex, and it should certainly be challenged in future theoretical studies. Even if this model of the relaxation time is able to reproduce well the experimental data with "only" five adjustable parameters (Fig. S29) and similar approaches have already been used for Dy/COT analogous SMMs,[10, 11] the physics of the present dynamics might be better described by alternative models, and thus the current analysis should be taken with a great caution as any similar modeling of the relaxation for SMMs.

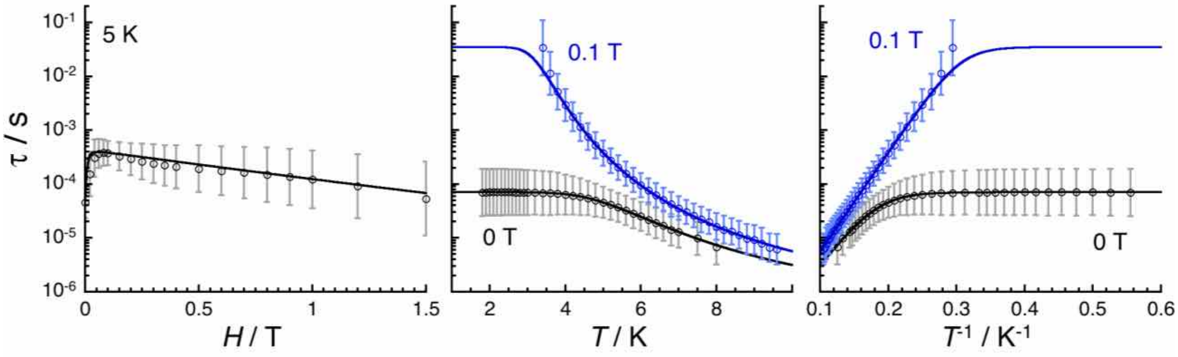

Fig. S29 Relaxation time variation for **3-Dy** as a function of the applied magnetic field at 5 K between 0 and 1.5 T (left) and as a function of the temperature between 1.8 and 10 K plotted as τ vs. T (center) and τ vs. T^{-1} (right) at zero (black open dots) and 0.1 T (blue open dots) dc fields (semi-logarithm plots). The reported relaxation time was estimated from the generalized Debye fits of the ac susceptibility data (Figs. 6, S23, S25, and S26). Estimated standard deviations of the relaxation time (vertical solid bars) have been calculated from the α parameters of the generalized Debye fit (Figs. S23a, S25a, and S26a) and the log-normal distribution as described in reference.[8] The solid lines are the best fit discussed in the text.

The temperature dependence of the magnetization relaxation time for **5-Er** and its ESD (Fig. S30) were extracted from the experimental ac susceptibility data shown in Fig. 7 and their fit to the generalised Debye model (Fig. S27).[7, 8] When applying a magnetic field at 27 K, the characteristic frequency of the relaxation mode stays unchanged suggesting that the magnetization relaxation is dominated by an Orbach-like process in this temperature range (Equation 1; among the different processes, Orbach-like relaxation is usually the less field dependent). Nevertheless, the $ln(\tau)$ versus T^{-1} plot (right part of Fig. S30) is not perfectly linear revealing a departure from a simple thermally activated process. A second relaxation pathway should thus be considered. In zero-dc field, only Raman and QTM are active processes (Equation 2) but only a model considering Raman and Orbach-like relaxations was able to fit all the experimental data (Fig. S30). The best set of parameters are $\tau_0 = 1.3(6)\times10^{-8}$ s, $\Delta/k_B = 287(16)$ K, $C = 1.4(9)\ 10^{-12}$ s^{-1} K^{-n} and $n = 10.4(3)$ (n is in relative good agreement with what is expected for the two-phonon second-order Raman relaxation for a Kramers ion).[12-14] It is worth mentioning that the characteristics of the Orbach-like process are indeed very similar to those estimated in related Er/COT complexes.[10, 15, 16]

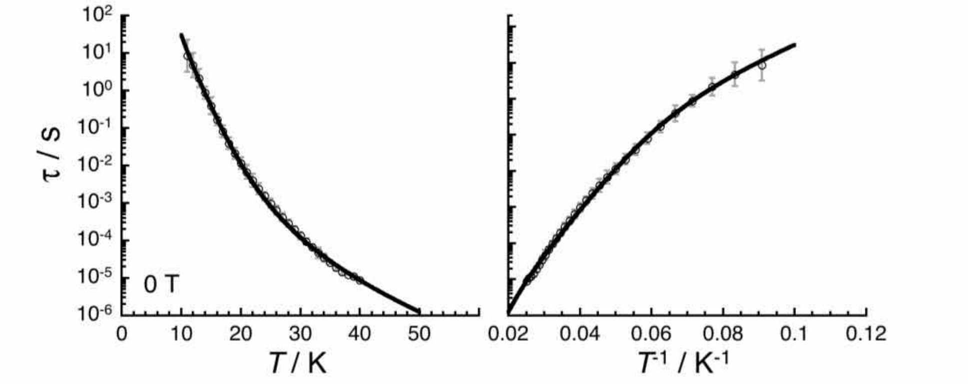

Fig. S30 Relaxation time variation for **5-Er** as a function of the temperature between 1.85 and 60 K plotted as τ vs. T (left) and τ vs. T^{-1} (right) at zero dc field (semi-logarithm plots). The reported relaxation time was estimated from the generalized Debye fits of the ac susceptibility data shown in Fig. 7. Estimated standard deviations of the relaxation time (vertical solid bars) have been calculated from the α parameters of the generalized Debye fit (Fig. S27) and the log-normal distribution as described in reference.[8] The solid line is the best fit discussed in the text.

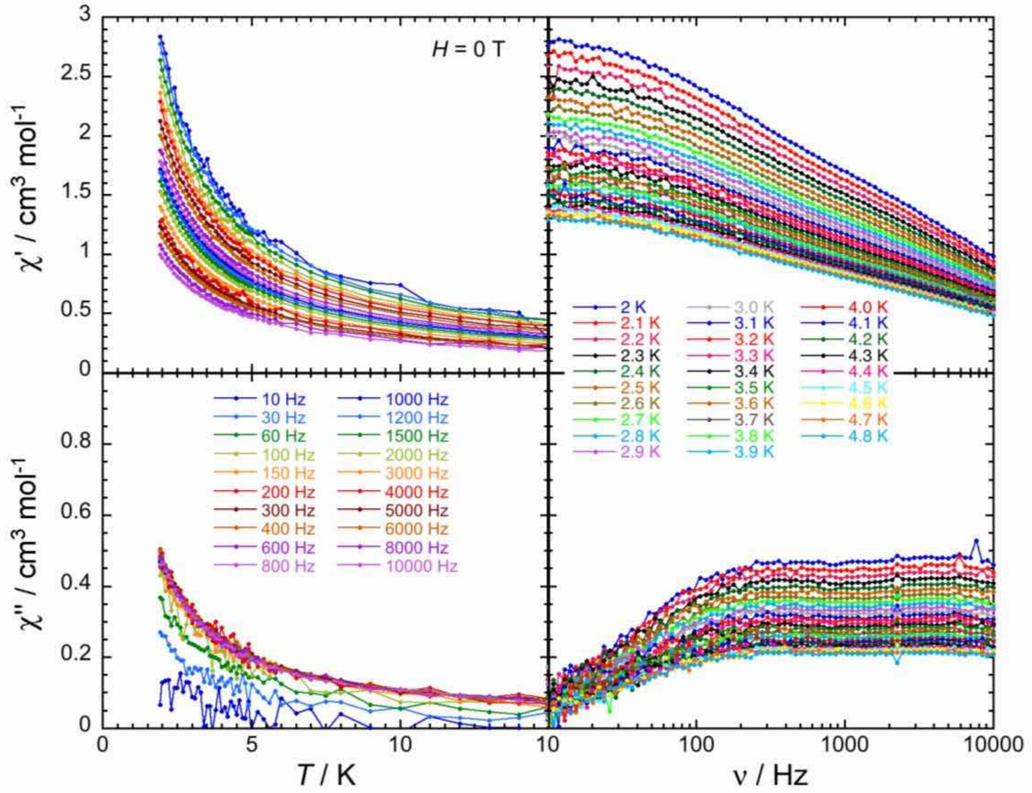

Fig. S31 In-phase (top) and out-of-phase (bottom) components of the molar ac magnetic susceptibility of **6-Tm** measured as a function of temperature at different frequencies (left) and as a function of frequency at different temperatures (right) in zero dc-field.

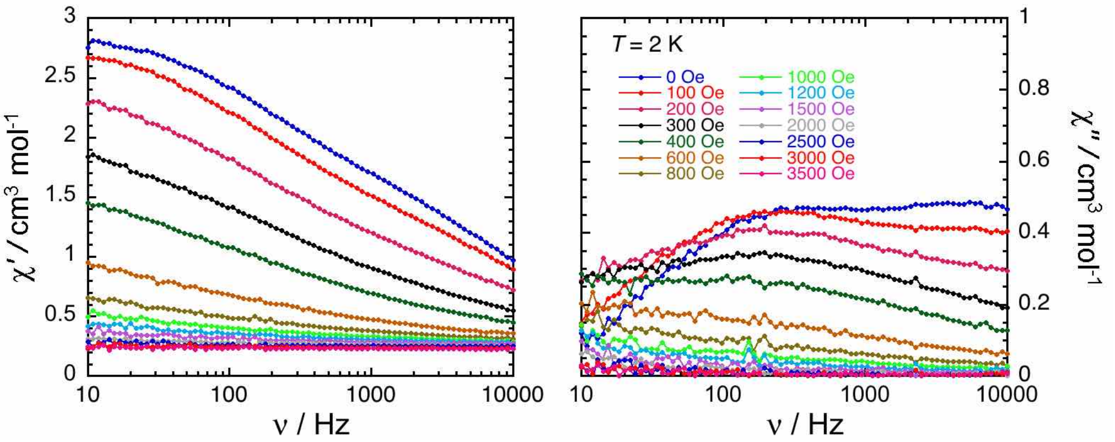

Fig. S32 ac frequency dependences (between 10 and 10000 Hz) of the real (χ', top) and imaginary (χ'', bottom) parts of the ac susceptibility for **6-Tm** at 2 K and under an applied dc field varying between 0 and 0.35 T.

VI. Computational Methods

The positions of hydrogen atoms in **1**–**7** were optimized with Grimme's composite PBEh-3C[17] method using the ORCA electronic structure package, version 5.[18-20] The equilibrium structures were then subjected to single point evaluations at the PBE0[21] and strongly-contracted NEVPT2(n,7)[22-24] levels using the RIJCOSX[25-29] approximation, where n is the relevant number of f-electrons in the complex. Scalar relativistic corrections were accounted for with the Zeroth-Order Regular Approximation (ZORA). The lanthanide centers were modeled with the SARC2-ZORA-QZVP[30-33] basis set, and all other atoms were treated with the ZORA-def2-TZVP basis set. Natural bond orbital analysis was performed on top of the converged PBE0 wavefunctions using NBO 7.0.[34]

Magnetic properties were evaluated using state-averaged CASSCF(n,7) and NEVPT2(n,7) wavefunctions, where state-averaged orbitals were used for each state in the NEVPT2 treatments (the so-called canonstep 0 in ORCA terminology). Full intermediate coupling was used for each complex. Spin-orbit coupling was included with quasi-degenerate perturbation theory (QDPT) using the SA-CASSCF wavefunction and strongly contracted NEVPT2 diagonal energies.[35] Ground state multiplet analysis was performed for CASSCF results with help of SINGLE_ANISO[36-38] approach as implemented in ORCA. Relativistic effects were included by using the spin-orbit mean field operator.

Table S13 Energy spectrum of |M$_J$| states for ground state multiplets of **2–7** calculated at the CASSCF(*n*,7) level. Columns in red are non-Kramers ions and the |M$_J$| labels are on the right, while blue columns are Kramers ions with |M$_J$| labels on the left

|M$_J$|	**2-Tb**	**3-Dy**	**4-Ho**	**5-Er**	**6-Tm**	**7-Yb**	|M$_J$|
	$^7F_6$	$^6H_{15/2}$	$^5I_8$	$^4I_{15/2}$	$^3H_6$	$^2F_{7/2}$	
15/2		986.5	515.2	0.0			8
13/2		244.3	351.9	189.2			**7**
11/2	636.2	28.5	137.1	409.9	0.0		6
9/2	696.6	0.0	0.0	526.7	696.8		5
7/2	848.6	45.5	10.9	513.4	872.4	174.9	4
5/2	407.5	98.2	78.6	412.1	860.5	0.0	3
3/2	180.6	154.7	193.0	291.7	822.2	553.3	2
1/2	45.0	134.4	291.1	214.2	780.7	907.5	1
	0.0		329.3		761.5		0

Table S14 Magnetic properties of the two lowest energy |M$_J$| states in the ground state multiplet for **2–7** at the CASSCF(*n*,7) level. θ is the angle between the g_z axes, and *ζ* is the SOC constant calculated at the NEVPT2(*n*,7) level of theory

	2-Tb	**3-Dy**	**4-Ho**	**5-Er**	**6-Tm**	**7-Yb**
|M$_J$|	0	9/2	9/2	15/2	6	5/2
g_x	0	0.0206	$3.1e^{-7}$	$6.9e^{-7}$	0.0	0.0117
g_y	0	0.0890	$4.1e^{-7}$	$8.1e^{-7}$	$6.0e^{-8}$	0.0350
g_z	0	12.5883	10.9591	17.9424	13.9776	5.7310
|M$_J$|	1	11/2	7/2	13/2	5	7/2
g_x	0	0.0104	$3.7e^{-7}$	0.0019	0.0	0.0113
g_y	$8.0e^{-8}$	0.0328	$4.2e^{-7}$	0.0019	$5.0e^{-8}$	0.0115
g_z	3.3132	14.3627	12.7992	15.5256	11.5846	7.9985
θ (°)	N/A	22.6	38.8	0.17	1.3	5.4
ζ (cm^{-1})	1698.81	1894.24	2105.13	2332.05	2576.56	2831.59

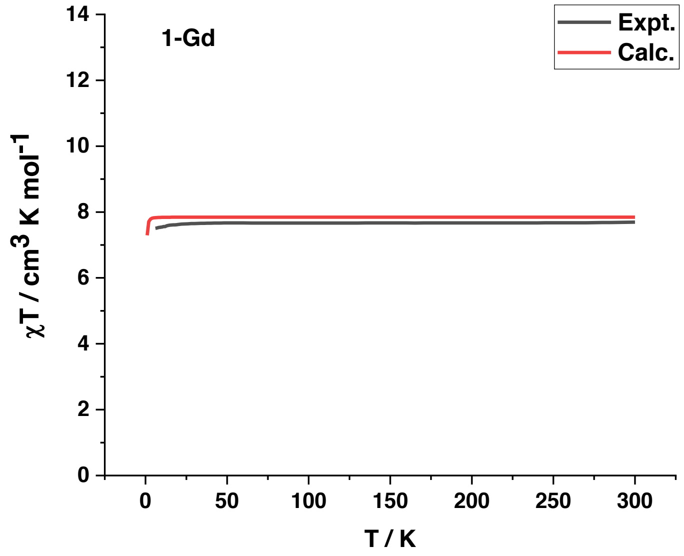

Fig. S33 Calculated (red) and experimental χT curves for **1-Gd**.

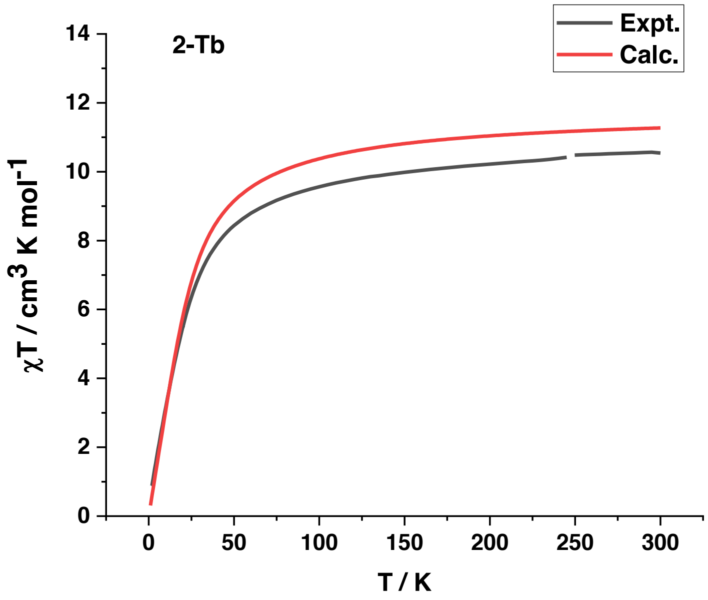

Fig. S34 Calculated (red) and experimental χT curves for **2-Tb**.

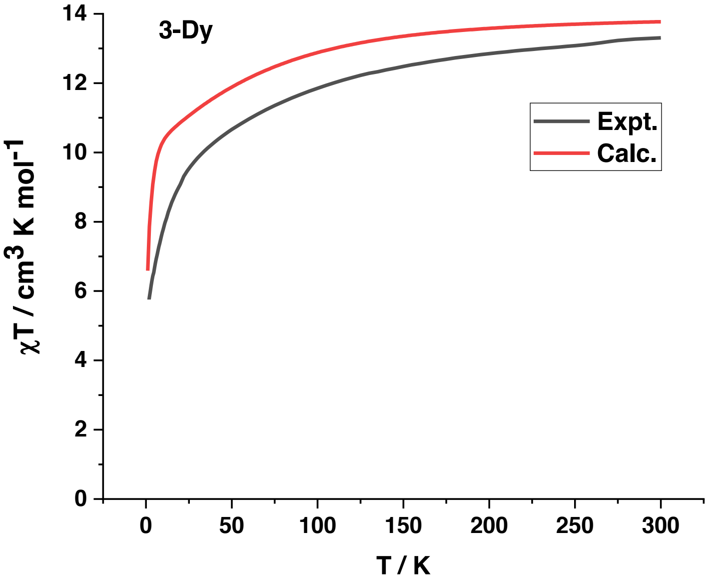

Fig. S35 Calculated (red) and experimental χT curves for **3-Dy**.

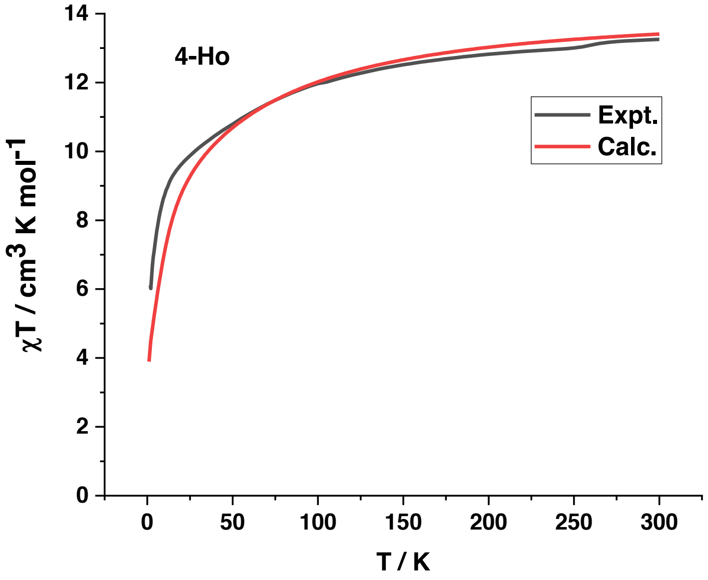

Fig. S36 Calculated (red) and experimental χT curves for **4-Ho**.

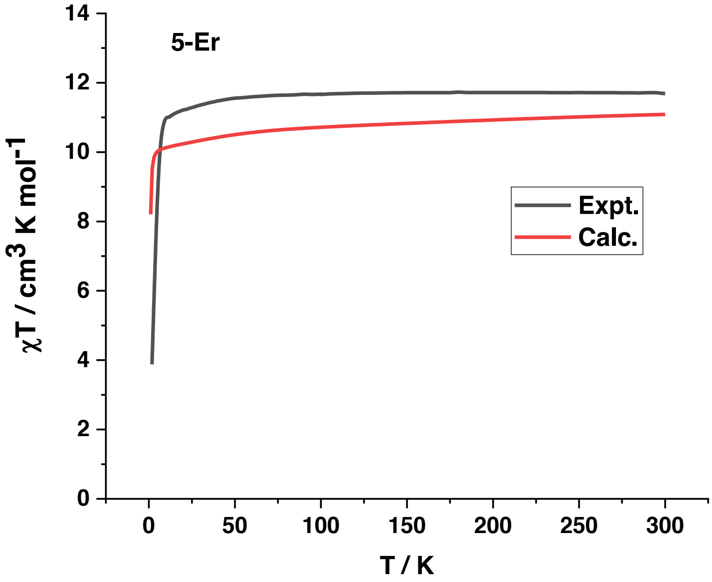

Fig. S37 Calculated (red) and experimental χT curves for **5-Er**.

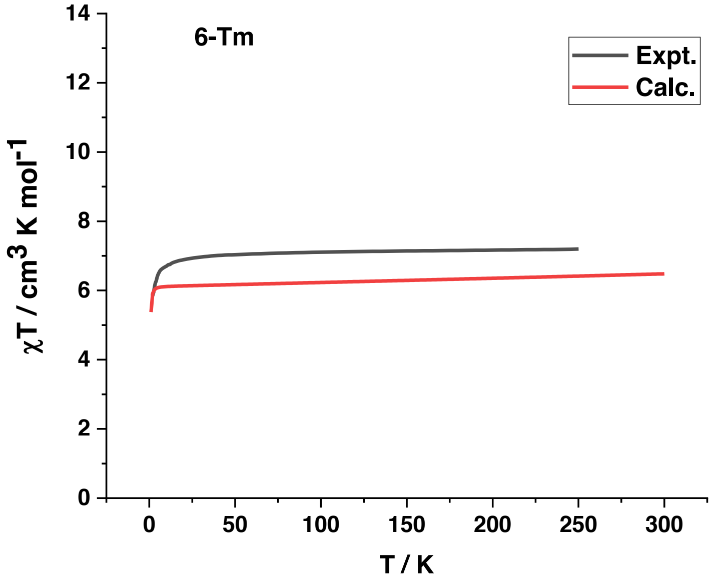

Fig. S38 Calculated (red) and experimental χT curves for **6-Tm**.

VII. References

1. N. V. Kozhemyakina, J. Nuss and M. Jansen, *Z. Anorg. Allg. Chem.*, 2009, **635**, 1355-1361.
2. Z. Zhou, J. Greenough, Z. Wei and M. A. Petrukhina, *Acta Crystallogr., Sect. C: Struct. Chem.*, 2017, **73**, 420-423.
3. SAINT; part of Bruker APEX3 software package (version 2017.3-0): Bruker AXS, 2017.
4. SADABS; part of Bruker APEX3 software package (version 2017.3-0): Bruker AXS, 2017.
5. G. M. Sheldrick, *Acta Crystallogr.*, 2015, **A71**, 3-8.
6. G. M. Sheldrick, *Acta Crystallogr.*, 2015, **C71**, 3-8.
7. K. S. Cole and R. H. Cole, *J. Chem. Phys.*, 1941, **9**, 341-351.
8. D. Reta and N. F. Chilton, *PCCP*, 2019, **21**, 23567-23575.
9. D. Gatteschi, R. Sessoli and J. Villain, *Molecular Nanomagnets*, Oxford University Press, Oxford, 2006.
10. L. Ungur, J. J. Le Roy, I. Korobkov, M. Murugesu and L. F. Chibotaru, *Angew. Chem. Int. Ed.*, 2014, **53**, 4413-4417.
11. J. J. Le Roy, M. Jeletic, S. I. Gorelsky, I. Korobkov, L. Ungur, L. F. Chibotaru and M. Murugesu, *J. Am. Chem. Soc.*, 2013, **135**, 3502-3510.
12. K. N. Shrivastava, *Phys. Stat. Sol. B*, 1983, **117**, 437-458.
13. J. H. Van Vleck, *Phys. Rev.*, 1940, **57**, 426-447.
14. A. Abragam and B. Bleaney, *Electron Paramagnetic Resonance of Transition Ions*, Dover, New York, 1986.
15. J. J. Le Roy, L. Ungur, I. Korobkov, L. F. Chibotaru and M. Murugesu, *J. Am. Chem. Soc.*, 2014, **136**, 8003-8010.
16. K. R. Meihaus and J. R. Long, *J. Am. Chem. Soc.*, 2013, **135**, 17952-17957.
17. S. Grimme, J. G. Brandenburg, C. Bannwarth and A. Hansen, *J. Chem. Phys.*, 2015, **143**, 054107.
18. F. Neese, *Wiley Interdiscip. Rev.: Comput. Mol. Sci.*, 2012, **2**, 73-78.
19. F. Neese, *ORCA – An Ab Initio, DFT and Semiempirical SCF-MO Package, Ver. 4.0*, Max Planck Institute for Chemical Energy Conversion, Mülheim a. d. Rurh, Germany, 2017.
20. F. Neese, *Wiley Interdiscip. Rev.: Comput. Mol. Sci.*, 2018, **8**, e1327.
21. A. D. Becke, *J. Chem. Phys.*, 1993, **98**, 1372-1377.
22. C. Angeli, R. Cimiraglia and J.-P. Malrieu, *Chem. Phys. Lett.*, 2001, **350**, 297-305.
23. C. Angeli, R. Cimiraglia, S. Evangelisti, T. Leininger and J. P. Malrieu, *J. Chem. Phys.*, 2001, **114**, 10252-10264.
24. C. Angeli, B. Bories, A. Cavallini and R. Cimiraglia, *J. Chem. Phys.*, 2006, **124**, 054108.
25. F. Neese, *J. Comput. Chem.*, 2003, **24**, 1740-1747.
26. F. Neese, F. Wennmohs, A. Hansen and U. Becker, *Chem. Phys.*, 2009, **356**, 98-109.
27. S. Kossmann and F. Neese, *Chem. Phys. Lett.*, 2009, **481**, 240-243.
28. R. Izsák and F. Neese, *J. Chem. Phys.*, 2011, **135**, 144105.
29. D. Ganyushin, N. Gilka, P. R. Taylor, C. M. Marian and F. Neese, *J. Chem. Phys.*, 2010, **132**, 144111.
30. D. Aravena, F. Neese and D. A. Pantazis, *J. Chem. Theory Comput.*, 2016, **12**, 1148-1156.

31. J. Chmela and M. E. Harding, *Mol. Phys.*, 2018, **116**, 1523-1538.
32. F. Weigend, *PCCP*, 2006, **8**, 1057-1065.
33. F. Weigend and R. Ahlrichs, *PCCP*, 2005, **7**, 3297-3305.
34. E. D. Glendening, J. K. Badenhoop, A. E. Reed, J. E. Carpenter, J. A. Bohmann, C. M. Morales, P. Karafiloglou, C. R. Landis and F. Weinhold, *NBO 7.0*, University of Wisconsin, Madison, WI, 2018.
35. D. Ganyushin and F. Neese, *J. Chem. Phys.*, 2006, **125**, 024103.
36. L. F. Chibotaru and L. Ungur, *J. Chem. Phys.*, 2012, **137**, 064112.
37. N. Iwahara, L. Ungur and L. F. Chibotaru, *Phys. Rev. B*, 2018, **98**, 054436.
38. L. Ungur and L. F. Chibotaru, *Chem. - Eur. J.*, 2017, **23**, 3708-3718.